

# Periodically driven Rydberg chains with staggered detuning

Bhaskar Mukherjee<sup>1</sup>, Arnab Sen<sup>2</sup>, K. Sengupta<sup>2</sup>

<sup>1</sup> *Department of Physics, University College London, Gower Street, London WC1E 6BT, UK.*

<sup>2</sup> *School of Physical Sciences, Indian Association for the Cultivation of Science, Jadavpur, Kolkata 700032, India*

(Dated: January 3, 2022)

We study the stroboscopic dynamics of a periodically driven finite Rydberg chain with staggered ( $\Delta$ ) and time-dependent uniform ( $\lambda(t)$ ) detuning terms using exact diagonalization (ED). We show that at intermediate drive frequencies ( $\omega_D$ ), the presence of a finite  $\Delta$  results in violation of the eigenstate thermalization hypothesis (ETH) via clustering of Floquet eigenstates. Such clustering is lost at special commensurate drive frequencies for which  $\hbar\omega_d = n\Delta$  ( $n \in \mathbb{Z}$ ) leading to restoration of ergodicity. The violation of ETH in these driven finite-sized chains is also evident from the dynamical freezing displayed by the density-density correlation function at specific  $\omega_D$ . Such a correlator exhibits stable oscillations with perfect revivals when driven close to the freezing frequencies for initial all spin-down ( $|0\rangle$ ) or Neel ( $|\mathbb{Z}_2\rangle$ , with up-spins on even sites) states. The amplitudes of these oscillations vanish at the freezing frequencies and reduces upon increasing  $\Delta$ ; their frequencies, however, remains pinned to  $\Delta/\hbar$  in the large  $\Delta$  limit. In contrast, for the  $|\bar{\mathbb{Z}}_2\rangle$  (time-reversed partner of  $|\mathbb{Z}_2\rangle$ ) initial state, we find complete absence of such oscillations leading to freezing for a range of  $\omega_D$ ; this range increases with  $\Delta$ . We also study the properties of quantum many-body scars in the Floquet spectrum of the model as a function of  $\Delta$  and show the existence of novel mid-spectrum scars at large  $\Delta$ . We supplement our numerical results with those from an analytic Floquet Hamiltonian computed using Floquet perturbation theory (FPT) and also provide a semi-analytic computation of the quantum scar states within a forward scattering approximation (FSA). This allows us to provide qualitative analytical explanations of the above-mentioned numerical results.

## I. INTRODUCTION

The physics of non-equilibrium quantum systems has been studied extensively in recent years<sup>1-8</sup>. The theoretical studies in the field have been boosted by possibility of experimental realization using ultracold atom platforms<sup>9-13</sup>. Out of the several possible drive protocols that could be used to take a quantum system out of equilibrium, periodic drives have attracted a lot of recent attention<sup>6-8</sup>. For such protocols characterized by a time period  $T$ , the unitary evolution operator  $U(t, 0)$  governs the dynamics of the system. At times  $t = nT$ , (where  $n \in \mathbb{Z}$ )  $U$  can be written in terms of the Floquet Hamiltonian  $H_F$ :  $U(nT, 0) = \exp[-iH_F nT/\hbar]$ , where  $\hbar$  is Planck's constant. Thus the stroboscopic dynamics of the system is completely governed by its Floquet Hamiltonian<sup>8</sup>.

The interest in such drive protocols stems from several interesting physical phenomena which occurs in periodically driven systems. These include drive-induced non-trivial topology<sup>14-16</sup>, dynamical localization<sup>17-20</sup>, dynamical phase transitions<sup>21-23</sup>, realization of time crystals<sup>24-26</sup>, dynamical freezing<sup>27-32</sup> and the possibility of tuning ergodicity property of the driven system<sup>33</sup>. More recently, some of these properties have also been investigated in the context of quasiperiodically<sup>34-36</sup> and aperiodically<sup>36</sup> driven systems.

A central paradigm for understanding the behavior of non-integrable many-body systems described by local Hamiltonians that are driven out of equilibrium comes from the eigenstate thermalization hypothesis (ETH)<sup>37-40</sup>. ETH postulates that the reduced density matrix of any eigenstate with finite energy density is ther-

mal in the thermodynamic limit, the corresponding temperature being determined by its energy density. ETH has also proved successful in explaining properties of non-integrable systems in the presence of a periodic drive; here eigenstates of the Floquet Hamiltonian play a similar role<sup>40</sup>.

The violation of ETH in many-body systems can occur via several routes<sup>32,33,41-60</sup>. For example, ETH does not hold for integrable models where the presence of an extensive number of additional conserved quantities makes the system non-ergodic. Moreover, a loss of ergodicity and hence violation of ETH may also happen due to strong disorder when a system enters a many-body localized (MBL) phase<sup>41-45</sup>. Such violation may also occur due to Hilbert space fragmentation where the system Hilbert space organizes into dynamically disconnected sectors<sup>57-60</sup>.

Another weaker version of ETH violation has also been found in Rydberg atom systems<sup>32,33,46-49,52</sup>. Experiments on such systems showed coherent long-lived oscillation of density of Rydberg excitations during evolution starting from a Neel state with one Rydberg excitation at every even ( $|\mathbb{Z}_2\rangle = |..12_j, 0_{2j+1}, 1_{2j+2}, \dots\rangle$ ) or odd ( $|\bar{\mathbb{Z}}_2\rangle = |..1_{2j-1}, 0_{2j}, 1_{2j+1}, \dots\rangle$ ) site; in contrast, ETH predicted thermalization occurred when the dynamics started from the Rydberg vacuum state ( $|0\rangle = |..0_j, 0_{j+1}, \dots\rangle$ )<sup>13</sup>. The reason for such ETH violating oscillations were traced to the existence of a special class of eigenstates called quantum scars<sup>32,33,46-56</sup>. These are many-body eigenstates with finite energy density but anomalously low entanglement entropy. Consequently, dynamics starting from an initial state which has large overlap with them do not show thermalization. The role of such states in periodically driven Rydberg chain has

also been analyzed<sup>32,33</sup>; it was shown that their presence may lead to the possibility of drive-frequency induced tuning ergodicity property of these chains<sup>33</sup>, presence of subthermal steady states, and the phenomenon of dynamical freezing<sup>32</sup>. These properties do not have any analogue for scar-induced dynamics following a quench.

More recently, there have been several studies on possible role of confinement in condensed matter systems. The concept of confinement in 1D quantum electrodynamics is well-known; it was shown that such systems are characterized by a parameter  $\theta$  which is related to the background electric field. For  $\theta = \pi$ , the system is deconfined and charge excitations can propagate; for other values of  $\theta$ , these excitations are confined<sup>61,62</sup>. Such ideas have also been applied to the simulation of lattice gauge theories (LGTs) using ultracold atom platforms<sup>63–68</sup>, Ising like chains<sup>69</sup>, and Rydberg chains with staggered detuning described by the Hamiltonian<sup>46,70–73</sup>

$$H_{\text{ryd}} = -w \sum_j \tilde{\sigma}_j^x - \frac{1}{2} \sum_j (\lambda + \Delta(-1)^j) \sigma_j^z \quad (1)$$

Here  $\Delta > 0$  and  $\lambda$  denote the amplitude of staggered and uniform detuning respectively,  $w > 0$  is the coupling strength between ground and excited states of the Rydberg atoms,  $\sigma_j^z = 2\hat{n}_j - 1$  is related to the number operator  $\hat{n}_j$  for a Rydberg excitations on site  $j$ . The Hamiltonian given by Eq. 1 is to be supplemented by a constraint that two adjacent sites can not both have Rydberg excitations. Thus the model has a Rydberg blockade radius of one lattice site. This constraint is implemented using the projected spin operators  $\tilde{\sigma}_j^x = P_{j-1} \sigma_j^x P_{j+1}$ , where  $P_{j-1} = (1 - \sigma_{j-1}^z)/2$ . The dynamics of such Rydberg chains was studied in context of quench protocols in Ref. 70,71. It was observed that the presence of the confinement terms leads to slow dynamics of the Rydberg atoms. However, periodic drive protocols for such chains have not been studied so far.

In this work, we study a periodically driven Rydberg chain with a staggered detuning term. Here we consider the uniform detuning parameter  $\lambda$  to be a periodic function of time given by

$$\begin{aligned} \lambda(t) &= \lambda_0 \quad t \leq T/2 \\ &= -\lambda_0 \quad t > T/2 \end{aligned} \quad (2)$$

where  $T = 2\pi/\omega_D$ ,  $\omega_D$  is the drive frequency and we focus in the regime of large drive amplitude:  $\lambda_0 \gg \Delta, w$ . In the rest of this work we focus on the dynamics of the density-density correlation function  $O_{j2} = \langle \hat{n}_j \hat{n}_{j+2} \rangle$  of these driven Rydberg atoms and the half-chain entanglement entropy  $S_{L/2}$  of their Floquet eigenstates. We use ED to study the properties of  $S_{L/2}$  and  $O_{j2}$  numerically. We supplement our numerical finding by comparing them with those obtained from an analytic, albeit perturbative, Floquet Hamiltonian derived using Floquet perturbation theory (FPT) and also present a calculation of some Floquet eigenstates using forward scattering approximation (FSA) applied to the analytic Floquet Hamiltonian.

The main results that we obtain from such a study are as follows. First, we show, via study of  $S_{L/2}$ , the presence of clustering of Floquet eigenstates in these systems for strong staggered detuning and at intermediate frequencies leading to violation of ETH. These clusters can be classified into two categories. The first type, dubbed as primary clusters, is a result of near-integrable nature of the system for large staggered detuning. The second type of clusters occurs within each primary cluster at a much smaller quasienergy scale. We show that these secondary clusters result from an emergent conservation law found earlier in non-driven staggered Rydberg chains<sup>52</sup>. Second, we also show that the secondary clustering is destroyed, leading to ergodicity restoration within each primary cluster, at commensurate drive frequencies  $\hbar\omega_D = n\Delta$ , where  $n$  is an integer; this allows drive-induced tuning of ergodicity property of the Floquet eigenstates within each primary cluster. Third, we show that for almost all intermediate drive frequencies,  $O_{22}$  does not reach its ETH predicted steady state value; this phenomenon is seen for  $|\mathbb{Z}_2\rangle$ ,  $|0\rangle$  and the  $|\bar{\mathbb{Z}}_2\rangle$  initial states. For dynamics starting from  $|\mathbb{Z}_2\rangle$  and  $|0\rangle$  initial states, we find specific drive frequencies for which the system is dynamically frozen;  $O_{22}$  remains pinned to its initial values at these frequencies. Around these freezing frequencies,  $O_{22}$  displays oscillatory behavior around its initial values with perfect revivals; the amplitudes of these oscillations vanish as the freezing frequency is approached and reduces as  $\Delta$  is increased. In contrast, the frequency of these oscillation are pinned to  $\Delta/\hbar$  for a wide range of  $\Delta$  in the intermediate and large  $\Delta$  regime. We provide a semi-analytic explanation of this phenomenon. Fourth, in contrast to the above cases, for the  $|\bar{\mathbb{Z}}_2\rangle$  initial state,  $O_{22}$  remains frozen over a range of frequencies leading to a dynamically frozen phase. We provide a qualitative explanation for this phenomenon; our analysis shows that for odd  $j$ ,  $O_{j2}$  will have a frozen phase for dynamics starting from  $|\mathbb{Z}_2\rangle$ . This dichotomy is a direct consequence of the  $Z_2$  (between even and odd sites) symmetry breaking due to the presence of the staggered detuning. Fifth, we study the fate of the quantum many-body scars in the Floquet eigenspectrum as a function of the staggered detuning. For small  $\Delta$ , these scars have almost equal overlap with both the Neel states; in contrast, we find that scars with  $E_F < 0$  ( $E_F > 0$ ) have stronger overlap with  $|\mathbb{Z}_2\rangle$  ( $|\bar{\mathbb{Z}}_2\rangle$ ). For large enough  $\Delta$ , the mid spectrum scars ( $E_F \simeq 0$ ) do not show significant overlap with either of the Neel states; instead we show that these represent a separate type of scar states exhibiting high overlap either with number states with broken  $Z_4$  symmetry ( $|\mathbb{Z}_4\rangle$ ) or with states having single Rydberg excitation ( $|1\rangle$ ). These scar states results in long-time coherent oscillations for dynamics starting from  $|\mathbb{Z}_4\rangle$  or  $|1\rangle$  initial states and are therefore qualitatively different from their counterparts in the PXP model<sup>47</sup>. We also present a computation of the scars at small and intermediate  $\Delta$  using a FSA formalism<sup>74</sup>.

The plan of the rest of the paper is as follows. In

Sec. II, we obtain the analytic Floquet Hamiltonian using FPT. This is followed by Sec. III where we study the structure of the Floquet eigenspectrum for strong staggered detuning and discuss the resultant clustering. Next, in Sec. IV, we analyze the dynamical freezing of  $O_{22}$  and its dynamics near the freezing points. This is followed by Sec. V where we discuss the change in properties of the quantum many-body scars in the Floquet eigenspectra as  $\Delta$  is tuned from small to large values. Finally, we summarize our main results and conclude in Sec. VI. Some details of the calculation are presented in the appendix.

## II. DERIVATION OF THE FLOQUET HAMILTONIAN

In this section, we derive an analytic Floquet Hamiltonian for the driven Rydberg atoms described by Eq. 1 in the presence of the drive protocol given by Eq. 2. To this end, we shall focus on the limit  $\lambda_0 \gg \Delta, w$ ; however, no restriction is placed on the relative magnitude of  $\Delta$  and  $w$ . For the rest of this section, we shall set  $\hbar = 1$ .

In what follows, we shall use FPT to obtain the Floquet Hamiltonian<sup>9,32</sup>. Since  $\lambda_0 \gg \Delta, w$ , we treat the uniform detuning term exactly and rewrite Eq. 1 as  $H = H_0(t) + H_1 + H_2$  where

$$\begin{aligned} H_0(t) &= -\frac{1}{2}\lambda(t)\sum_j\sigma_j^z, \\ H_1 &= -\frac{1}{2}\sum_j\Delta(-1)^j\sigma_j^z, \quad H_2 = -w\sum_j\tilde{\sigma}_j^x. \end{aligned} \quad (3)$$

---


$$\langle m|U_1(T,0)|n\rangle = iT\sum_m\left(\sum_j\frac{\Delta}{2}(-1)^j\langle m|\sigma_j^z|m\rangle\langle m|\delta_{mn} + \sum_{s_j=\pm 1}\frac{4iw}{\lambda_0 T}\sin\frac{\lambda_0 T}{4}e^{i\lambda_0 T s_j}|m\rangle\langle m+s_j|\delta_{n,m+s_j}\right) \quad (6)$$


---

Using Eq. 6, one obtains the first order Floquet Hamiltonian, given by  $H_F^{(1)} = iU_1(T,0)/T$  to be

$$H_F^{(1)} = H_1 - w_r\sum_j(\cos\gamma\tilde{\sigma}_x + \sin\gamma\tilde{\sigma}_y), \quad w_r = \frac{w\sin\gamma}{\gamma} \quad (7)$$

where  $\gamma = \lambda_0 T/4$ . We note that the second term in  $H_F^{(1)}$ , obtained in Refs. 32,33, vanishes at  $\gamma = n\pi$  (or  $\lambda_0 = 2n\omega_D$ ) for non-zero integer  $n$ ; thus at these points, we expect the effect of the staggered detuning term ( $H_1$ ) to be particularly strong.

It turns out that there is no second order contribution

We shall treat  $H_1$  and  $H_2$  perturbatively. This leads to the evolution operator

$$\begin{aligned} U_0(t,0) &= T_t\left[e^{-i\int_0^t H_0(t')dt'}\right] \\ &= e^{i\lambda_0 t\sum_j\sigma_j^z/2} \quad t \leq T/2 \\ &= e^{i\lambda_0(T-t)\sum_j\sigma_j^z/2} \quad t \geq T/2, \end{aligned} \quad (4)$$

We note that  $U_0(T,0) = I$  which leads to  $H_F^{(0)} = 0$ . Also, for subsequent computation, we define the states  $|m\rangle$  as eigenstates of  $H_0$  that have  $m$  up-spins and  $L-m$  down-spins. Such states need to obey the constraint imposed by the model; thus  $m_{\max} = L/2$  is the maximum number of up-spins.

Next, we consider the first order correction to the Floquet Hamiltonian given, within FPT, by

$$U_1(T,0) = -i\int_0^T dt_1 U_0^\dagger(t_1,0)(H_1 + H_2)U_0(t_1,0) \quad (5)$$

To evaluate  $U_1$ , we note that  $H_1$  commutes with  $U_0$ . Moreover, the contribution from  $H_2$  has already been obtained in Refs. 32,33. From these we find,

to  $H_F$  since

$$\begin{aligned} U_2(T,0) &= -\int_0^T dt_1 U_0^\dagger(t_1,0)(H_1 + H_2)U_0(t_1,0) \\ &\quad \times \int_0^{t_1} dt_2 U_0^\dagger(t_2,0)(H_1 + H_2)U_0(t_2,0) \\ &= U_1(T,0)^2/2 \end{aligned} \quad (8)$$

Eq. 8 can be obtained from a straightforward computation; however, it can also be checked as follows. First we note that the terms  $\sim H_1$  in the expression of  $U_2$  commutes with  $U_0$ . This indicates that the term originating from  $H_1^2$  in  $U_2(T,0)$  must trivially satisfy Eqn. 8. Second, we recall that it is known<sup>32,33</sup> that the term  $\sim H_2^2$  does not yield any second order contribution to  $H_F$ . This is due to the presence of a symmetry noted

in Ref. 33. For  $\Delta = 0$ , it was shown that  $\{Q, H_F\} = 0$ , where  $Q = \prod_j \sigma_j^z$ ; consequently, there can be no terms with product of even number of  $\tilde{\sigma}_j^\pm$  operators in  $H_F$ . Moreover, a straightforward computation shows that the contribution from all terms which involve both  $H_1$  and  $H_2$  also vanish due to commutation of  $H_1$  with  $U_0$ . Thus we have  $H_F^{(2)} = 0$ .

Finally, we compute the third order term in the Floquet Hamiltonian. To this end, we consider the third order contribution to  $U$ , given by

$$\begin{aligned} U_3(T, 0) &= i \int_0^T dt_2 U_0^\dagger(t_1, 0) (H_1 + H_2) U_0(t_1, 0) \\ &\quad \times \int_0^{t_1} dt_2 U_0^\dagger(t_2, 0) (H_1 + H_2) U_0(t_2, 0) \\ &\quad \times \int_0^{t_2} dt_3 U_0^\dagger(t_3, 0) (H_1 + H_2) U_0(t_3, 0). \end{aligned} \quad (9)$$

To obtain the third order Floquet Hamiltonian, we first note that the commutation of  $H_1$  with  $U_0$  ensures that there is no third order contribution to  $H_F$  from the term with three  $H_1$  operators. The first non-trivial contribution to the third order  $H_F$  comes from the term in Eq. 9 which has two  $H_1$  and one  $H_2$  operators. The contribution of this term to  $U_3(T, 0)$  can be computed as charted in details in Ref. 32. The result is

$$\begin{aligned} U_{3a}(T, 0) &= \frac{i\Delta_0^2 w}{4} \sum_{j_1, j_2, j_3} \sum_{s=\pm} (-1)^{j_1+j_2} (2c_{1s} \sigma_{j_1}^z \sigma_{j_2}^z \tilde{\sigma}_{j_3}^s \\ &\quad + c_{2s} \sigma_{j_1}^z \tilde{\sigma}_{j_3}^s \sigma_{j_2}^z) \quad (10) \\ c_{1\pm} &= \pm T^3 \frac{-i \pm 2\gamma(1 \pm 2i\gamma) - ie^{\pm 2i\gamma} (2\gamma^2 - 1)}{32\gamma^3} \\ c_{2\pm} &= \pm T^3 \frac{i \mp 2\gamma - ie^{\pm 2i\gamma} (2\gamma^2 + 1)}{16\gamma^3} \end{aligned}$$

The structure of  $U_{3a}$  shows that it is necessary to categorize the terms into two groups. The first constitutes the case where at least one of the  $j_i$ s are different from the other two. For these,  $U_{3a}(T, 0)$  either vanishes or can be written as

$$\begin{aligned} U_{3a}(T, 0) &= \frac{i\Delta_0^2 w}{4} \sum_{j_1 \neq j_2 \neq j_3} \sum_{s=\pm} (-1)^{j_1+j_2} (2c_{1s} + c_{2s}) \\ &\quad \times \sigma_{j_1}^z \sigma_{j_2}^z \tilde{\sigma}_{j_3}^s = \frac{U_1(T, 0)^3}{3!} \quad (11) \end{aligned}$$

where we have used the fact that  $2c_{1s} + c_{2s} = iT^2(\exp[i\lambda_0 T s] - 1)/(\lambda_0 s)$  for  $s = \pm 1$ . Thus such terms do not contribute to  $H_{F3}$ . However, when  $j_1 = j_2 = j_3$ , we find that the last term in Eqn. 10 acquires a negative sign due to the anticommutation of  $\sigma_j^z$  and  $\tilde{\sigma}_j^s$ . This leads to

$$U_{3a}(T, 0) = \frac{i\Delta_0^2 w}{4} \sum_j \sum_{s=\pm} (2c_{1s} - c_{2s}) \tilde{\sigma}_j^s \quad (12)$$

Comparing this with  $U_1(T, 0)^3/3!$ , we find that there is a non-trivial contribution to the Floquet Hamiltonian given by

$$H_{F1}^{(3)} = \frac{w\Delta_0^2}{2T} \sum_j (c_{2+} \tilde{\sigma}_j^+ + \text{h.c.}) \quad (13)$$

This term leads to a frequency dependent renormalization of the coefficient of  $w$  in the first order Floquet Hamiltonian.

The next contribution to the Floquet Hamiltonian comes from the terms in Eqn. 9 with two  $H_2$  and one  $H_1$  operators. The calculation of this term,  $U_{3b}(T, 0)$ , follows a similar route as that followed in Ref. 32 and leads to

$$\begin{aligned} U_{3b}(T, 0) &= \frac{i\Delta_0 w^2}{2} \sum_{j_1, j_2, j_3} \sum_{s_1, s_2=\pm} (-1)^{j_3} (2d_{1s_1 s_2} \tilde{\sigma}_{j_1}^{s_1} \tilde{\sigma}_{j_2}^{s_2} \sigma_{j_3}^z + d_{2s_1 s_2} \tilde{\sigma}_{j_1}^{s_1} \sigma_{j_3}^z \tilde{\sigma}_{j_2}^{s_2}) \quad (14) \\ d_{1++} &= T^3 \frac{-(i/4 + \gamma) + ie^{2i\gamma}(i + 2\gamma) + e^{12i\gamma}(3i/4 + 2\gamma)}{32\gamma^3}, \\ d_{1+-} &= T^3 \frac{\gamma(2 - i\gamma) - \gamma e^{2i\gamma} - i(1 - e^{2i\gamma})/2}{16\gamma^3} \\ d_{2++} &= T^3 \frac{i/4 - \gamma + 3e^{4i\gamma}/4 + e^{2i\gamma}(-i + 2\gamma)}{16\gamma^3}, \quad d_{2+-} = \frac{T^3}{8\gamma^3} \left( \frac{1}{2} \sin 2\gamma - \gamma \cos 2\gamma \right) \quad (15) \end{aligned}$$

and  $d_{a\pm\pm} = d_{a\mp\mp}^*$  for  $a = 1, 2$ . The argument leading to the Floquet Hamiltonian is similar to the one discussed earlier and only the on-site terms in  $U_{3b}$  contribute to

$H_F^{(3)}$ . The final result is

$$H_{F2}^{(3)} = -\frac{w^2 \Delta_0}{T} \sum_j (-1)^j (d_{2+-} \tilde{\sigma}_j^+ \sigma_j^z \tilde{\sigma}_j^- + \text{h.c.}) \quad (16)$$

Note that the action of  $H_{F2}^{(3)}$  on any eigenstate of  $\sigma_j^z$  is same as that of  $-\sigma_j^z$ . Thus this term can be considered as a correction of the staggered detuning term in the first order Floquet Hamiltonian. From Eq. 14, we find that for  $\tan 2\gamma > 2\gamma$ , this correction is negative and leads to a reduction in the magnitude of the on-site detuning.

The final term in the Floquet Hamiltonian comes from the term in Eq. 9 which has three  $H_2$  operators. This term has already been computed in Ref. 32; for completeness, we write the contribution of this term to  $H_F$  here. This is given by

$$H_{F3}^{(3)} = \sum_j A_0 [(\tilde{\sigma}_{j-1}^+ \tilde{\sigma}_{j+1}^+ + \tilde{\sigma}_{j+1}^+ \tilde{\sigma}_{j-1}^+) \tilde{\sigma}_j^- - 6\sigma_j^+] + \text{h.c.}$$

$$A_0 = [e^{6i\gamma} + 3e^{2i\gamma}(1 + 4i\gamma) + 2(1 - 3e^{12i\gamma})]$$

$$\times \frac{w^3 T^2 e^{-12i\gamma}}{192i\gamma^3} \quad (17)$$

This term contains a three-spin term as well as a higher-order correction to the first order Floquet term  $\sim w$ .

This completes our derivation of the Floquet Hamiltonian for the driven Rydberg chain with staggered detuning to third order in Floquet perturbation theory. In subsequent sections, we shall use this along with numerical results to analyze the properties of the driven chain.

### III. STRONG STAGGERED DETUNING

In this and the next two sections, we present the main results of our study obtained by exact numerics and compare them to that obtained from the analytic Floquet Hamiltonian derived in Sec. II. In the present section, we shall restrict ourselves to the strong staggered detuning limit ( $\Delta \geq w$ ), while other parameter regimes will be explored in Secs. IV and V.

The exact numerical results that we present are obtained using ED on finite sized chain as follows. We first numerically diagonalize  $H[\pm\lambda_0] = H_0[\pm\lambda_0] + H_1 + H_2$  (Eq. 3) to obtain their energy eigenvalues  $\epsilon_a^\pm$  and eigenvectors  $|\xi_a^\pm\rangle$ . The evolution operator for the square pulse protocol (Eq. 2) can then be written as

$$U(T, 0) = e^{-iH_F[-\lambda_0]T/(2\hbar)} e^{-iH_F[\lambda_0]T/(2\hbar)}$$

$$= \sum_{a,b} c_{ab}^{-+} e^{-i(\epsilon_a^- + \epsilon_b^+)T/(2\hbar)} |\xi_a^-\rangle \langle \xi_b^+| \quad (18)$$

The result of such a computation is shown in Figs. 1 and 2 for  $\Delta = 1.2w$ . From Fig. 1, we find that the Hilbert space is ergodic at high drive frequencies for which  $w_r \simeq w$ . In contrast, as seen from Fig. 2, it fragments into several clusters at intermediate  $\omega_D$ . We dub these clusters as primary clusters. Their origin can be straightforwardly understood as follows.

We note that the leading terms in the Floquet Hamilto-

where  $c_{ab}^{-+} = \langle \xi_a^- | \xi_b^+ \rangle$ . We then numerically diagonalize the unitary matrix  $U$  to obtain its eigenvalues  $\lambda_n = \exp[-iE_n^F T/\hbar]$  and eigenvectors  $|\chi_n\rangle$ . The exact Floquet Hamiltonian of the system can then be obtained as

$$H_F = \sum_n E_n^F |\chi_n\rangle \langle \chi_n| \quad (19)$$

In what follows, we shall use Eq. 19 for numerical computation of the Floquet Hamiltonian. Most the numerical results in the rest of this section, unless explicitly mentioned otherwise, correspond to  $\lambda = 15$  and  $w = 1$ .

#### A. Clustering of Floquet Eigenstates

In this subsection, we discuss the structure of the Hilbert space spanned by Floquet eigenstates of the driven staggered Rydberg chain. To this end, we plot the half-chain entanglement entropy,  $S_{L/2}$ , of these eigenstates as a function of their quasienergy  $E_F$ . The details of the numerical procedure used for this computation is same as that charted in Ref. 33. The first step involves writing down the density matrix  $\rho_n = |\chi_n\rangle \langle \chi_n|$  corresponding to the  $n^{\text{th}}$  Floquet eigenstate. One then integrates out the contribution to this state from Fock states residing on one half of the chain; such an operation has to be carried out numerically without violating the constraint condition as detailed in Ref. 33. This leads to the reduced density matrix  $\rho_n^{\text{red}}$ . The von-Neumann entanglement entropy is then computed from  $\rho_n^{\text{red}}$  following the standard prescription:  $S_{L/2}^{(n)} \equiv S_{L/2} = -\text{Tr}[\rho_n^{\text{red}} \ln \rho_n^{\text{red}}]$ . For finite-sized periodically driven systems, the prediction of ETH for  $S_{L/2}$  is given by the Page formula:  $S_{L/2}^{\text{Page}} = \ln \text{HSD} - 1/2$ , where HSD denotes Hilbert space dimension of the half-chain with open boundary condition, and  $\text{HSD} = 377$  for  $L = 24$ .

nian given by  $H_{F1}$ . For  $\lambda T/\hbar \leq 1$  ( $\omega_D = 100w/\hbar$ ), when  $w_r \sim w$ , the amplitude of the staggered and the PXP terms in  $H_{F1}$  are comparable and their eigenstates span the entire Hilbert space as expected for a non-integrable model. This behavior is shown in the left panel of Fig. 1 and is further highlighted by plotting the expectation



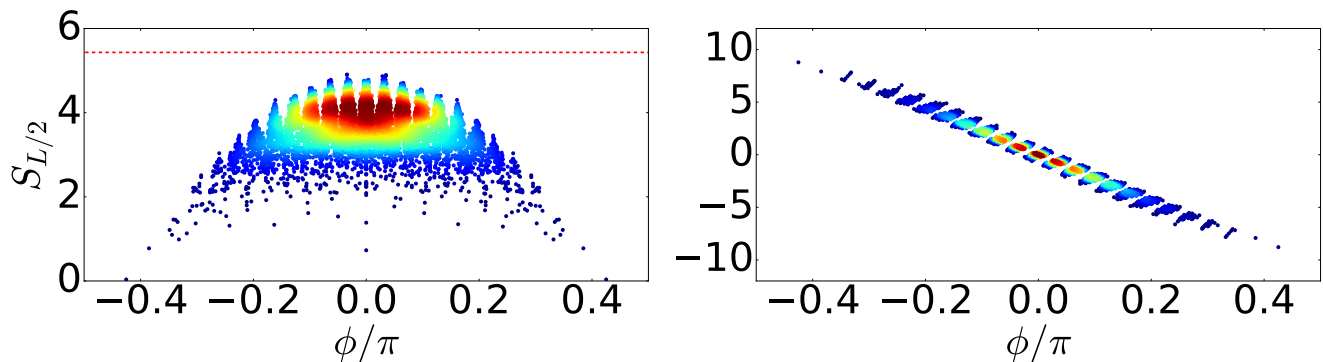


FIG. 1: Left: Plot of  $S_{L/2}$  as a function of  $\phi = E_F T/\hbar$  for  $\omega_D = 100w/\hbar$ . The red dotted line is the ETH predicted Page value of  $S_{L/2}$ . Right panel: Plot of  $\langle Z_\pi \rangle$  for Floquet eigenstates as a function of  $\phi$  for same  $\omega_D$ . For both plots  $L = 24$ ,  $\Delta/w = 1.2$ , and  $\lambda/w = 15$ . All energies are scaled in units of  $w$  and frequencies in units of  $w/\hbar$ . The color scheme indicates higher density of states for warmer colors. See text for details.

value of

$$Z_\pi = \frac{1}{2} \sum_j (-1)^j \sigma_j^z \quad (20)$$

for these states, as shown in the right panel of Fig. 1. We find that the quasienergy difference between the states with different  $\langle Z_\pi \rangle$  are  $O(w)$ ; hence  $w_r \sim w$  can hybridize states with different  $\langle Z_\pi \rangle$  leading to ergodicity.

In contrast, for  $\omega_D \sim 3.5w/\hbar$  and  $3.65w/\hbar$ ,  $w_r \ll w, \Delta$ . In this limit, the model is near-integrable and the eigenstates cluster into groups as shown in the top panels of Fig. 2. Each of these group have states with definite values  $\langle Z_\pi \rangle$  and dimensionless quasienergy

$$\phi = \frac{E_F T}{\hbar} \simeq -\frac{\Delta T}{\hbar} \langle Z_\pi \rangle \quad (21)$$

as shown in the bottom panels panel of Fig. 2. It is crucial to note here that  $\phi$  is  $2\pi$  periodic; thus Floquet eigenstates with quasienergy outside the range  $-\pi \leq \phi \leq \pi$  have to be folded back, using this periodicity, to the first Floquet-Brillouin zone. The primary clustering is therefore a consequence of near-integrability of  $H_F$  for small  $w_r/\Delta$ .

The eigenstates within the central primary cluster seen in the top panel of Fig. 2 has  $\langle Z_\pi \rangle = \pm 3n$  while the other

clusters have  $\langle Z_\pi \rangle = \pm 3n + 1$  and  $\pm 3n + 2$  where  $n$  is an integer. The number of such primary clusters can be deduced from the fact that for the parameter regime of these plots  $\Delta/(\hbar\omega_D) \sim 1/3$ . Importantly,  $\Delta$  is still incommensurate to the drive frequency by a small amount (the exact commensuration occurs at  $\Delta = \omega_D/3 \sim 1.2w$ ) so that states within the same cluster are non-degenerate. This incommensuration can be parameterized by a dimensionless ratio given by

$$x = \frac{\hbar\omega_D}{\Delta} - 3. \quad (22)$$

For  $\Delta = 1.2$ ,  $x \simeq -0.0834$  for  $\omega_D = 3.5w/\hbar$  and  $0.04167$  for  $\omega_D = 3.65w/\hbar$ . The primary clusters, for  $w_r \ll \Delta$ , are separated with quasienergies  $\phi_1$  while the states within each cluster are separated by smaller quasienergy scale  $\phi_2$ , where

$$\begin{aligned} \phi_1 &= \delta E_1 T/\hbar \sim 2\pi/(3+x) \\ \phi_2 &= \delta E_2 T/\hbar \sim |x|2\pi/(3+x). \end{aligned} \quad (23)$$

In the parameter regime of our numerics, where  $w_r \ll \delta E_1$ , the primary clustering is not destroyed by  $w_r$  for finite sized chains with  $L \leq 24$ .

A closer inspection of the primary clusters reveal that each of them, with definite values of  $Z_\pi$ , exhibit further clustering. The left[right] panel of Fig. 3 shows such clustering for  $\omega_D = 3.5[3.65]w/\hbar$ . We dub this phenomenon as secondary clustering. The origin of such secondary

clustering can be understood via construction of an effective Floquet Hamiltonian in the regime  $w_r \sim \delta E_2 \ll \delta E_1$ . The analysis is same as what has been carried out in Ref. 52 and have been detailed in the appendix. Such a Hamiltonian, given by Eqs. A.4 and A.5, shows that  $w_r$  can

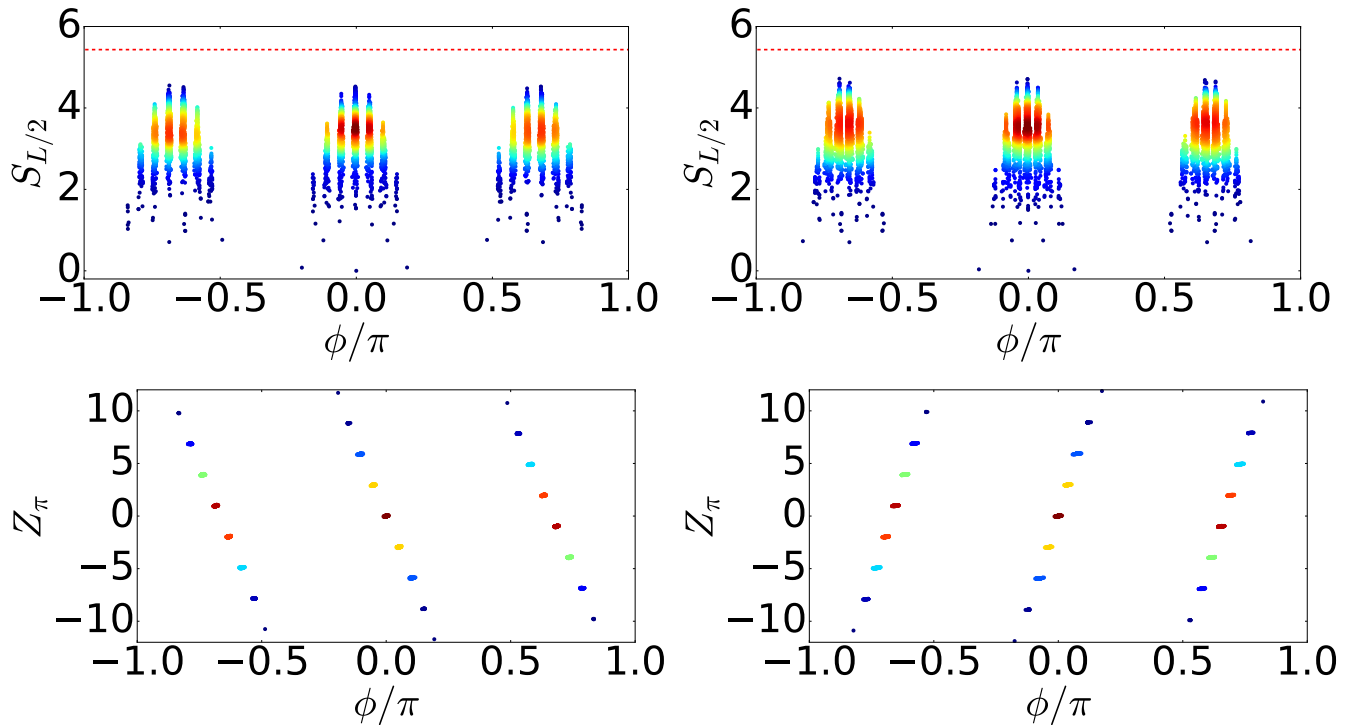


FIG. 2: Top left panel: Plot of  $S_{L/2}$  as a function of Floquet quasienergies  $\phi = E_F T/\hbar$  for  $\omega_D = 3.5w/\hbar$ . Top right panel: A similar plot for  $\omega_D = 3.65w/\hbar$ . Bottom left panel: Plot of  $\langle Z_\pi \rangle$  for Floquet eigenstates as a function of  $\phi$  for  $\omega_D = 3.5w/\hbar$ . Bottom right panel: Similar plot as the bottom left panel but for  $\omega_D = 3.65w/\hbar$ . For all plots  $L = 24$ ,  $\Delta = 1.2w$ , and  $\lambda = 15w$ . All energies are scaled in units of  $w$  and frequencies in units of  $w/\hbar$ . The color scheme is same as in Fig. 1 and the red dotted lines in the top panel indicate ETH predicted Page value of  $S_{L/2}$ . See text for details.

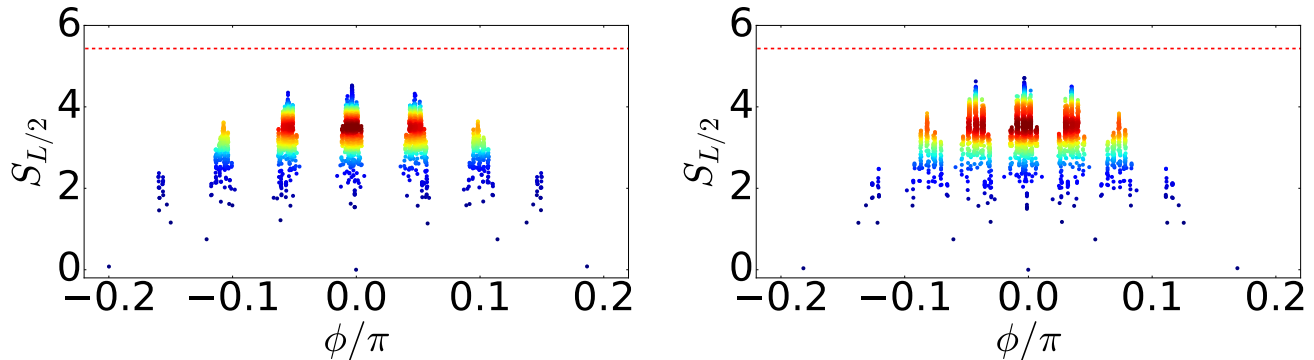


FIG. 3: Left panel: Plot of  $S_{L/2}$  as a function of Floquet quasienergies  $\phi = E_F T/\hbar$  within the central primary cluster for  $\omega_D = 3.5w/\hbar$ . Top right panel: A similar plot for  $\omega_D = 3.65w/\hbar$ . For all plots  $L = 24$ ,  $\Delta = 1.2w$ , and  $\lambda = 15w$ . All energies are scaled in units of  $w$  and frequencies in units of  $w/\hbar$ . The color scheme is same as in Fig. 1 and the red dotted lines in the top panel indicate ETH predicted Page value of  $S_{L/2}$ . See text for details.

have significant non-zero matrix elements only between states within each primary cluster. Moreover, as shown in Ref. 52, the presence of a finite  $w_r$  does not lead to ergodic structure within each primary cluster. Instead, a perturbative analysis, similar to that carried out in Ref. 52 and detailed in the appendix, indicates that the secondary clustering occurs due to an emergent conserved

quantity (Eq. A.5)

$$Y = - \sum_j (-1)^j P_{j-1} \sigma_j^z P_{j+1} \quad (24)$$

within each  $Z_\pi$  sector. These secondary clusters correspond to groups of states with same values of  $\langle Y \rangle$ . This can be clearly seen from Fig. 4 where  $\langle Y \rangle$  is plotted for eigenstates in each of the primary cluster. We find a definite value of  $\langle Y \rangle$  for all Floquet eigenstates both at

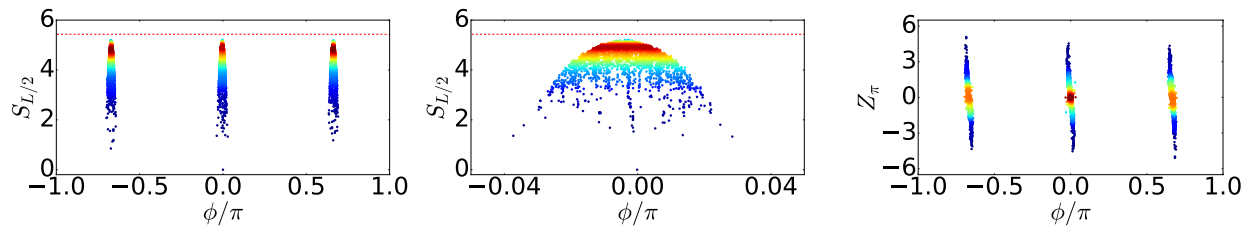


FIG. 5: Left panel: Plot of  $S_{L/2}$  as a function of  $\phi = E_F T/\hbar$  for  $\omega_D = 3.58w/\hbar$ . Central panel: A similar plot showing states within the primary cluster around  $E_F = 0$ . Right Panel: Plot of  $\langle Z_\pi \rangle$  as a function of  $\phi$ . For all plots  $\Delta/w = 1.2$ , and  $\lambda/w = 15$ . All energies are scaled in units of  $w$  and frequencies in units of  $w/\hbar$ . The color scheme is same as in Fig. 1 and the red dotted lines in the left and central panels indicate ETH predicted Page value of  $S_{L/2}$ . See text for details.

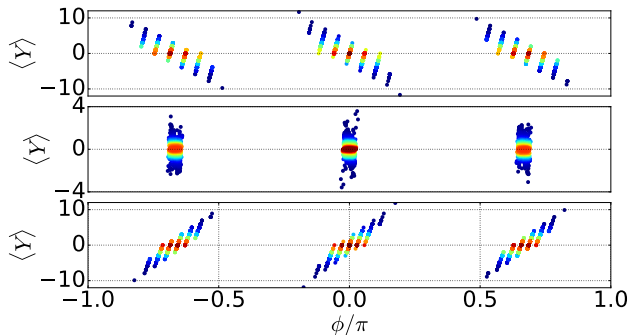


FIG. 4: Plot of  $\langle Y \rangle$  for the Floquet eigenstates as a function of  $\phi = E_F T/\hbar$  for  $\hbar\omega_D = 3.65w$  (top panel),  $3.58w$  (middle panel) and  $3.5w$  (bottom panel). For all plots  $L = 24$ ,  $\lambda/w = 15$ , and  $\Delta/w = 1.2$ . All energies are scaled in units of  $w$  and frequencies in units of  $w/\hbar$ . The color scheme is same as in Fig. 1 and the black dashed lines are guide to the eye. See text for details.

$\hbar\omega_D = 3.65w$  and  $3.5w$  as can be seen from the top and bottom panels of Fig. 4 respectively. We note that the emergence of  $Y$  relies on the perturbative parameter  $w_r/\delta E_2 \leq 1$ . Such a perturbation theory will break down for at the exact commensuration point where  $x$ , and hence  $\delta E_2$ , vanishes. This leads to loss of secondary clustering. At these commensuration points, the Floquet eigenstates can not be associated with a definite  $\langle Y \rangle$  value as can be seen from the middle panel of Fig. 4. We shall discuss this case in Sec. III B.

### B. Ergodicity restoration

In this section, we discuss the behavior of the driven chain when the amplitude of the staggered detuning is

---

In the presence of a non-zero  $w_r$ , within each cluster, the effective Floquet Hamiltonian is given by  $H'_1$ . For small  $w_r$ , the primary clustering still exists for finite  $L$ ,

commensurate with the drive frequency. To this end, we note that the Floquet Hamiltonian derived using FPT in Sec. II can be written as

$$\begin{aligned}
 H_F &= - \sum_j \Delta_r Z_\pi + H'_1 \\
 H'_1 &= -w_r \sum_j \tilde{\sigma}_j^x + H_{F3}^{(2)} + H_F^{(3)} + \dots \\
 \Delta_r &= \Delta \left[ 1 - \frac{w^2 T^2}{8\gamma^3} \left( \frac{1}{2} \sin 2\gamma - \gamma \cos 2\gamma \right) + \dots \right] \quad (25)
 \end{aligned}$$

where the ellipsis indicate higher order contribution to the Floquet Hamiltonian and  $\Delta_r$  denote the renormalized amplitude of the staggered term. We note that for  $\hbar\omega_D/\Delta_r = n$  where  $n \in \mathbb{Z}$ , one can write

$$U(T, 0) = e^{-iH_F T/\hbar} = e^{-i(H'_1 T + (2\pi/n)Z_\pi)/\hbar} \quad (26)$$

Thus the Floquet eigenstates can be organized into clusters of states with values of  $\langle Z_\pi \rangle = \pm 3n, \pm 3n + 1$  and  $\pm 3n + 2$ . This is seen in the top left panel of Fig. 5. We also note that each of the states in a given primary cluster shall have identical quasienergy at  $w_r = 0$  since  $x$ , and hence  $\delta E_2$ , vanishes. Thus in absence of  $w_r$ , they form a flat band and the Hilbert space comprises of three such flat bands with  $\delta E_1 = 0$  and  $\pm \hbar\omega_D/3$  in this limit. The number of such clusters depends on  $n$ ; this is exhibited in Fig. 6 where the structure of the states with  $n = 2$  and  $n = 4$  primary clusters are shown.

---

since  $w_r \ll \Delta$ . However, within each primary cluster,  $H_F^{\text{eff}} \simeq H'_1$  since  $\delta E_2 = 0$ . Thus the effective Floquet Hamiltonian for each primary cluster resembles a renor-



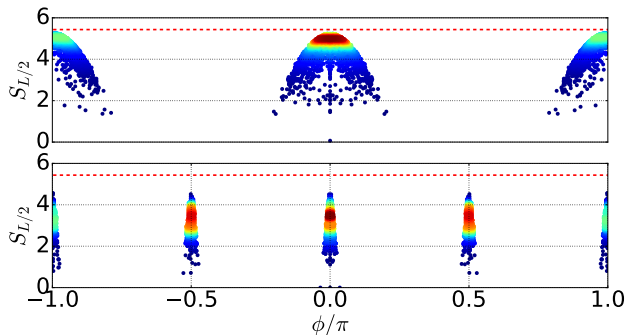


FIG. 6: Top Panel: Plot of  $S_{L/2}$  as a function of Floquet quasienergies  $\phi = E_F T / \hbar$  for  $\Delta/w = 1.8$  showing two primary clusters. Bottom panel: A similar plot for  $\Delta/w = 0.9$  showing four primary clusters. For both plots  $\hbar\omega_D/w = 3.6w$ , and  $\lambda/w = 15$ . All energies are scaled in units of  $w$  and frequencies in units of  $w/\hbar$ . The color scheme is same as in Fig. 1 and the red dotted lines indicate ETH predicted Page value of  $S_{L/2}$ . The black dashed lines are guide to the eye. See text for details.

malized PXP Hamiltonian along with higher order terms. The states within each primary cluster are therefore expected to have an ergodic structure with no secondary clustering. Moreover, as seen from the bottom panel of Fig. 5, they possess a continuous range of  $\langle Z_\pi \rangle$  values for any finite  $w_r$ . This property stems from strong hybridization between states with definite integer values of  $\langle Z_\pi \rangle$  in the presence of non-zero  $w_r$ . We note that the perturbative analysis derived in Ref. 52 leading to the emergent invariant  $Y$  responsible for the secondary clustering becomes invalid here since the perturbative parameter  $w_r/\delta E_2 \rightarrow \infty$  at the commensuration point. This expectation is validated from exact numerics as seen from the top right panel of Fig. 5 where the ergodic structure for states within the central primary cluster is shown. We note that each of the clusters contains both anomalous states with low  $S_{L/2}$  along with thermal states with high  $S_{L/2}$ . A similar behavior is expected for the  $s = \pm 1$  primary clusters.

The consequence of such ergodicity restoration within a primary cluster is also reflected in the steady state value of  $O_{22}$ ,  $O_{22}^{\text{DE}}$ , as shown in Fig. 7. The steady state value of  $O_{22}$ , in terms of the Floquet spectrum, is given by

$$O_{22}^{\text{DE}} = \sum_n |c_n^{\text{init}}|^2 \langle n | \hat{n}_2 \hat{n}_4 | n \rangle \quad (27)$$

where  $c_n^{\text{init}} = \langle n | \psi_0 \rangle$  and  $|\psi_0\rangle \equiv |\bar{Z}_2\rangle, |Z_2\rangle, \text{ or } |0\rangle$  is the overlap of the Floquet eigenstates  $|n\rangle$  with the initial state. We find that  $O_{22}^{\text{DE}}$  exhibits a sharp dip at the commensuration point when the dynamics starts from  $|Z_2\rangle$ ; in contrast it exhibits a smaller peak for  $|\bar{Z}_2\rangle$  initial state. In both cases, its value approaches close to that predicted by ETH. This is clearly a consequence of restoration of ergodicity within a primary cluster. As one varies the frequency away from the commensuration point,  $O_{22}^{\text{DE}}$

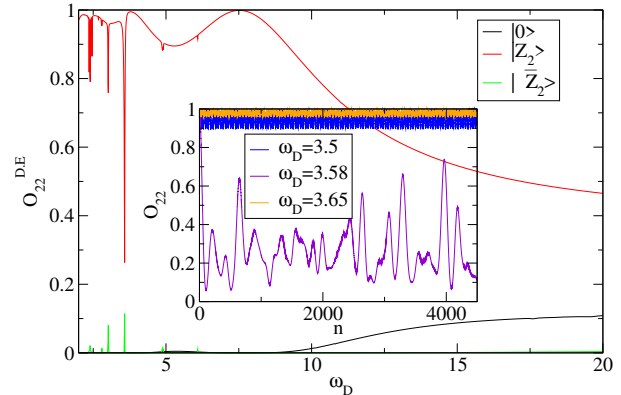


FIG. 7: Plot of the steady state value of  $O_{22} \equiv O_{22}^{\text{DE}}$  as a function  $\omega_D$  for  $\Delta/w = 1.2$  showing restoration of ergodicity at special frequencies. Such restoration is characterized by sharp dips in the  $O_{22}^{\text{DE}}$  value. The inset shows the dynamics of  $O_{22}$  starting from a  $|Z_2\rangle$  state as a function of  $n$  for commensurate ( $\hbar\omega_D/w = 3.58$ ) and slightly incommensurate ( $\hbar\omega_D/w = 3.65$  and  $\hbar\omega_D/w = 3.5$ ) drive frequencies. The coherent oscillations of  $O_{22}$  (shown above for  $\hbar\omega_D/w = 3.5$  and  $3.65$ ) seen at incommensurate frequencies are replaced by a slower approach to the steady state at exactly commensurate drive frequency ( $\hbar\omega_D/w = 3.58$ ). All energies (frequencies) are scaled in units of  $w(w/\hbar)$ . See text for details.

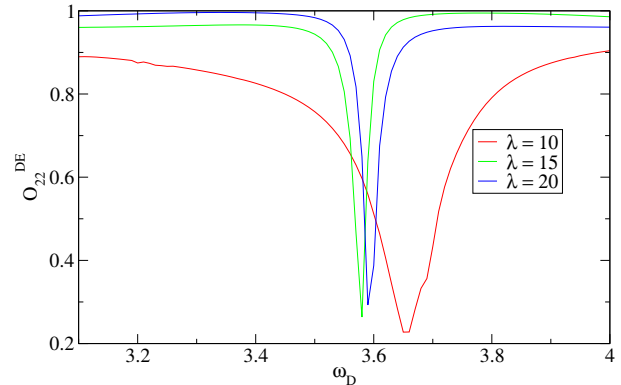


FIG. 8: Plot of the steady state value of  $O_{22} \equiv O_{22}^{\text{DE}}$  as a function  $\omega_D$  for  $\Delta/w = 1.2$  for several  $\lambda$  showing increase in width of the ergodic region as a function of  $\lambda$  around  $\hbar\omega_D/w = 3.58$ . All energies (frequencies) are scaled in units of  $w(w/\hbar)$ . See text for details.

deviates sharply from its ETH predicted value approximately around  $w_r \simeq \delta E_2$ . The sharpness of such deviation is a consequence of small  $w_r \simeq 0.045$  at  $\lambda = 15w$  and  $\hbar\omega_D = 3.58w$ . This can be controlled by varying  $\lambda$  (for a fixed  $\omega_D$ ) as seen in Fig. 8 displaying a significantly wider ergodic regime as a function of the drive frequency at  $\lambda = 5w$  and  $\lambda = 10w$ .

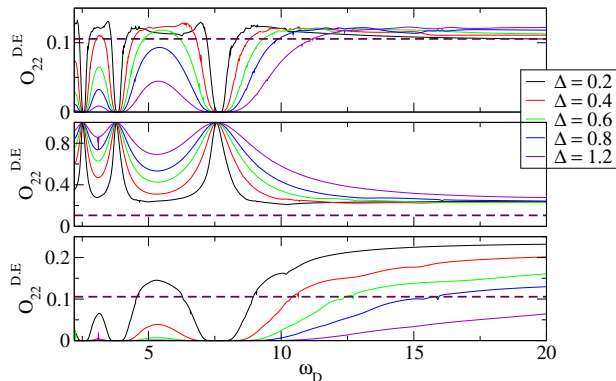


FIG. 9: Plot of the steady state value of  $O_{22} \equiv O_{22}^{\text{DE}}$  as a function of  $\omega_D$  starting from the  $|0\rangle$  (top panel),  $|\mathbb{Z}_2\rangle$  (middle panel) and  $|\bar{\mathbb{Z}}_2\rangle$  (bottom panel) states for several representative values of  $\Delta/w$  as shown. The black dashed lines indicate the ETH predicted value of  $O_{22}^{\text{DE}}$ . For all plots  $\lambda/w = 15$ . All energies are scaled in units of  $w$  and frequencies in units of  $w/\hbar$ . See text for details.

The stroboscopic evolution of  $O_{22}$  at these ergodicity restoring points do not display coherent oscillations as can be seen from the inset of Fig. 7; instead it displays a slow approach to the thermal steady state. We note that this is in contrast to the dynamics of  $O_{22}$  starting from  $|\mathbb{Z}_2\rangle$  for a renormalized PXP Floquet Hamiltonian. This difference can be understood as follows. Since  $w_r/\Delta \ll 1$ , the dynamics of  $O_{22}$  is dominated by terms which connects states within the same primary cluster. The matrix elements between any two such states, which differ by at least three flipped spins for  $\hbar\omega_D/\Delta_r \simeq 3$ , must involve at least  $O(w_r^3)$  term; consequently, the effective Hamiltonian for such dynamics is different from the renormalized PXP. Thus the scar-induced oscillations are not seen. Such an effective  $O(w_r^3)$  term naturally leads to a thermalization time which is  $O(w_r^{-3})$  and hence large.

#### IV. DYNAMICAL FREEZING

In this section, we present our results on the density-density correlation function  $O_{j2} = \langle \hat{n}_j \hat{n}_{j+2} \rangle$  with focus on dynamical freezing of these correlations at specific drive frequencies and their oscillations near these freezing frequencies. For all numerical results in this section, we shall choose  $j = 2$ . The discussion on the freezing phenomenon is given in Sec. IV A while the oscillation of  $O_{22}$  around the freezing point is analyzed in Sec. IV B.

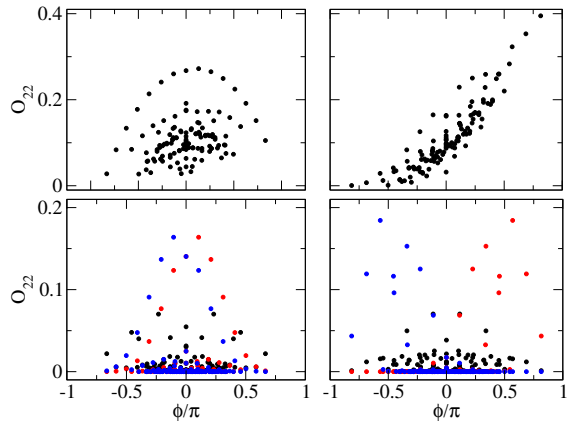


FIG. 10: Top left panel: Plot of  $O_{22}^{(m)} = \langle m | \hat{n}_2 \hat{n}_4 | m \rangle \equiv O_{22}$  corresponding to Floquet eigenstates  $|m\rangle$  as a function of their quasienergy  $\phi = E_F^{(m)} T/\hbar$  for  $\Delta/w = 0.1$ . Bottom left panel: Overlap of these eigenstates with  $|\mathbb{Z}_2\rangle$  (red dots),  $|\bar{\mathbb{Z}}_2\rangle$  (blue dots), and  $|0\rangle$  (black dots). Right panels: Same as the corresponding left panels but for  $\Delta/w = 1.2$ . All left panel plots have same Y axes range as their right panel counterparts. All plots correspond to  $L = 14$ ,  $\lambda/w = 15$  and  $\hbar\omega_D/w = 6.9$ . All energies are scaled in units of  $w$  and frequencies in units of  $w/\hbar$ . See text for details.

##### A. Freezing at special drive frequencies

We begin with a study of the behavior of  $O_{22}^{\text{DE}}$  as a function of  $\Delta/w$  as shown in Fig. 9. The plot shows its behavior for the initial Neel ( $|\mathbb{Z}_2\rangle$  and  $|\bar{\mathbb{Z}}_2\rangle$ ) and vacuum ( $|0\rangle$ ) states. It indicates strong deviation from the ETH predicted value  $O_{22}^{\text{ETH}} \simeq 0.11$  at intermediate drive frequencies. For the  $|0\rangle$  initial state,  $O_{22}^{\text{DE}}$  reaches its ETH predicted value at high drive frequencies where  $w_r \sim w \simeq \Delta$  as expected; in contrast, for the  $|\mathbb{Z}_2\rangle$  initial state,  $O_{22}^{\text{DE}}$  reaches a super-thermal value. The latter behavior can be attributed to the presence of scar states in the Floquet spectra with large overlap with the  $|\mathbb{Z}_2\rangle$  states<sup>32,33</sup>; we shall discuss these states in Sec. V. For either of these initial states,  $O_{22}^{\text{DE}}$ , in the high-frequency limit, is almost independent of  $\Delta$  as long as  $w \geq \Delta$ . In contrast, it depends strongly on  $\Delta$  for  $\hbar\omega_D \gg w$  and can take either superthermal or subthermal values for  $|\bar{\mathbb{Z}}_2\rangle$  initial state; this constitutes a stronger violation of ETH which can not be explained by presence of scars alone.

To see why this is the case, we note that  $\Delta/w \ll 1$ , the value of  $O_{22}^{\text{DE}}$  is expected to be identical irrespective of whether the starting state is  $|\mathbb{Z}_2\rangle$  or  $|\bar{\mathbb{Z}}_2\rangle$ . This situation is highlighted in the left panels of Fig. 10. The top left panel shows the expectation value  $O_{22}^{(m)} = \langle m | \hat{n}_2 \hat{n}_4 | m \rangle$  corresponding to the Floquet eigenstate  $|m\rangle$  as a function of their dimensionless quasienergy  $\phi = E_F^{(m)} T/\hbar$ . The bottom panel shows the overlap of the eigenstates  $|m\rangle$  with the initial states. For small  $\Delta/w = 0.2$ , we find that the largest value of  $O_{22}^{(m)}$  occurs for eigenstates  $|m\rangle$

which lie close to the middle of the Floquet spectrum ( $E_F \simeq 0$ ). Furthermore, near the middle of the Floquet spectrum, some of these states have significant overlap with  $|\mathbb{Z}_2\rangle$  while others have large overlap with  $|\bar{\mathbb{Z}}_2\rangle$  as can be seen the left bottom panel of Fig. 10. From Eq. 27, we find that this ensures that  $O_{22}^{\text{DE}}$  would be almost identical irrespective of whether the dynamics starts from  $|\mathbb{Z}_2\rangle$  or  $|\bar{\mathbb{Z}}_2\rangle$  initial states; in fact they have exactly identical values at  $\Delta = 0$ .

This situation drastically changes at large  $\Delta$ , where all the Floquet eigenstates with large values of  $O_{22}^{(m)}$  have quasienergy  $E_F > 0$  as shown in the top right panel of Fig. 10. Moreover, these eigenstates only have large overlap with  $|\mathbb{Z}_2\rangle$ . Consequently, the value of  $O_{22}^{\text{DE}}$  do not change appreciably for dynamics starting from  $|\mathbb{Z}_2\rangle$  as  $\Delta$  is increased; however, its value reduces drastically if the initial state is  $|\bar{\mathbb{Z}}_2\rangle$ . Thus with increasing  $\Delta$ ,  $O_{22}^{\text{DE}}$  drops rapidly to subthermal values and approaches zero for the  $|\bar{\mathbb{Z}}_2\rangle$  initial state; this leads to qualitatively different  $\Delta$ -dependence of  $O_{22}^{\text{DE}}$ .

In addition, the top and the middle panel plots of Fig. 9 indicate the presence of dynamical freezing at special values the drive frequencies  $\omega_D \simeq \lambda/(2n_0\hbar)$  (where  $n_0 \in \mathbb{Z}$ ) for which  $w_r \simeq 0$ . At these values, the initial states  $|0\rangle$ ,  $|\mathbb{Z}_2\rangle$  and  $|\bar{\mathbb{Z}}_2\rangle$  becomes approximate eigenstates of the Floquet Hamiltonian leading to freezing. The neighborhood of these freezing frequencies is marked by strong deviation from the ETH predicted value of  $O_{22}$  as shown in the top and middle panels of Fig. 9; this deviation increases with increasing  $\Delta$ . In contrast, for  $|\bar{\mathbb{Z}}_2\rangle$  initial state and for  $\Delta > w$ , the freezing extends over a range of frequencies, as seen in the bottom panel of Fig. 9.

## B. Oscillations around freezing frequencies

The stroboscopic dynamics of  $O_{22}$  as a function of  $n$  around the freezing frequencies is shown in the top panel Fig. 11. We find that  $O_{22}$  does not thermalize; instead, it displays long time oscillation with a fixed frequency  $\omega_{\text{osc}} \simeq \Delta/\hbar$ . We have checked this numerically for  $n > 1000$  cycles. The amplitude of these oscillation decrease as the freezing point is approached and also as  $\Delta$  is increased; it is a monotonically decreasing function of  $w_r/\Delta$ . However, the period of the oscillations remains constant for  $\Delta/w \geq 1$ , as shown in Fig. 12. A similar feature is seen from the fidelity  $\mathcal{F} = |\langle \mathbb{Z}_2 | \psi(nT) \rangle|^2$ , where  $|\psi(nT)\rangle$  denotes the many-body state at time  $t = nT$ , as shown in the bottom panel of Fig. 11. In contrast, the oscillation amplitude is close to zero for a wide range of frequencies around the freezing point when one starts from the  $|\bar{\mathbb{Z}}_2\rangle$  state.

The characteristics of these oscillations at large  $\Delta/w_r$  can be qualitatively understood as follows. Let us consider the evolution operator when  $\Delta_r \gg w_r$ . Clearly, in

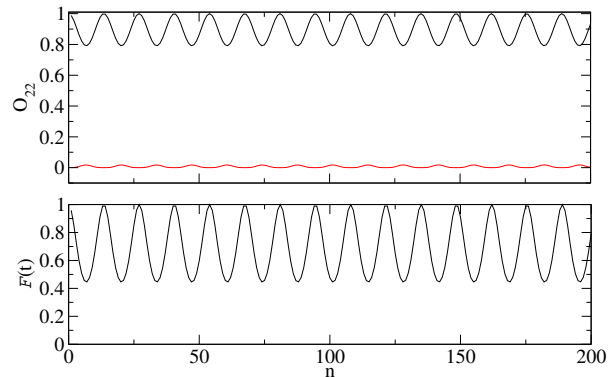


FIG. 11: Top panel: Plot of  $O_{22}$  as a function of the number of drive cycles  $n$  starting from the  $|0\rangle$  (red line),  $|\mathbb{Z}_2\rangle$  (black line). The bottom panel shows the plot of fidelity  $\mathcal{F}$  as a function of  $n$  for  $|\mathbb{Z}_2\rangle$  initial state. For all plots  $L = 14$ ,  $\lambda/w = 15$  and  $\hbar\omega_D/w = 6.9$ . All energies(frequencies) are scaled in units of  $w$  ( $w/\hbar$ ). See text for details.

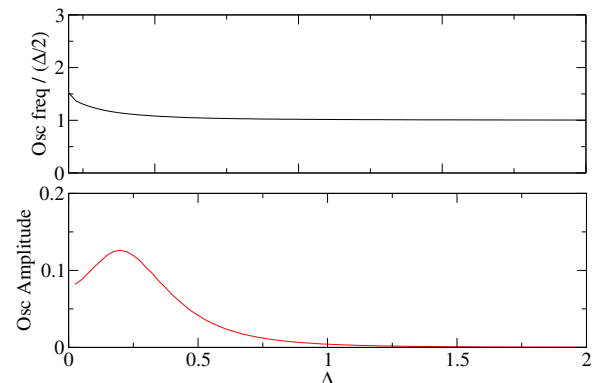


FIG. 12: Top panel: Plot of the frequency (top panel) and the amplitude (bottom panel) of coherent oscillation of  $O_{22}$  as a function of  $\Delta$  for  $\hbar\omega_D/w = 6.9$  and  $\lambda/w = 15$ . All energies(frequencies) are scaled in units of  $w$  ( $w/\hbar$ ). See text for details.

this limit, one can write

$$\begin{aligned}
 U(nT, 0) &= \sum_{\alpha} e^{-in\epsilon_{\alpha}^F T/\hbar} |\alpha\rangle\langle\alpha| \\
 \epsilon_{\alpha} &= E_0 + \alpha\Delta + O(w_r^2/\Delta^2) \\
 |\alpha\rangle &= \sum_p c_{p;q}^{\alpha} |p;q\rangle
 \end{aligned} \tag{28}$$

where  $E_0$  denotes the energy of the state  $|0\rangle$  for  $w_r = 0$  and any eigenstate  $|\alpha = \alpha_0\rangle$  of the Floquet Hamiltonian  $H_F$  is mapped to a state in the number basis  $|p;q\rangle = |p_0, q_0\rangle$  for  $w_r = 0$ . We note here that the states  $|p_0; q_0\rangle$  have  $p_0$  ( $q_0$ ) up-spins distributed on even (odd) sites of

the chain without violation of the constraint; these are eigenstates of  $H_F^{(1)}$  for  $w_r = 0$  with quasienergy

$$E = E_0 + (q_0 - p_0)\Delta. \quad (29)$$

Here we shall assume that  $c_{p_0+\mu; q_0}^{\alpha_0} \sim O((w_r/\Delta)^{|\mu|})$  for  $\mu = \pm 1, \pm 2, \dots$ ; thus for small  $w_r/\Delta$ ,  $|c_{p_0+\mu; q_0}^{\alpha_0}| \ll c_{p_0; q_0}^{\alpha_0}$  for any  $\alpha_0$ . A similar relation holds for  $c_{p_0; q_0+\mu}^{\alpha_0}$ .

Let us now consider the initial state  $|0\rangle$ . The wavefunction after  $n$  drive cycles can be obtained as

$$\begin{aligned} |\psi(nT)\rangle &= U(nT, 0)|0\rangle = \sum_{\alpha} c_{0;0}^{\alpha*} e^{-i\epsilon_{\alpha} nT/\hbar} |\alpha\rangle \\ &= \sum_{\alpha} \sum_{p,q} c_{0;0}^{\alpha*} c_{p,q}^{\alpha} e^{-i\epsilon_{\alpha} pT/\hbar} |p; q\rangle \end{aligned} \quad (30)$$

where  $c_{0;0}^{\alpha} = \langle p_0 = 0; q_0 = 0 | \alpha \rangle$ . Since the correlator  $O_{22}$  can receive finite contribution for states with  $p_0 > 2$  up-spins, we find that the leading contribution to  $O_{22}$  is given by

$$O_{22}^{(0)}(nT) \simeq |c_{0;0}^{0*} c_{2;0}^2 + c_{0;0}^{1*} c_{2;0}^1 e^{i\Delta nT/\hbar}|^2 \quad (31)$$

where we have retained only the leading order term in  $w_r/\Delta$  and used  $\epsilon_{\alpha_0} \simeq E_0 - (p_0 - q_0)\Delta$  (Eq. 28). This indicates that the oscillation amplitudes will decay with increasing  $\Delta$  as  $(w_r/\Delta)^4$ ; however the frequency of these oscillation will be pinned to  $\Delta$  as long as  $w_r \ll \Delta$ . The change in the oscillation frequency is expected to occur with reduction of  $\Delta$  when  $O((w_r/\Delta)^2)$  terms in the expression of  $\epsilon_{\alpha}$  becomes significant. The validation of this argument can be found in Fig. 12. We note that for  $\Delta_r \gg w_r$ , the presence of a large on-site term which is diagonal in the Fock basis leads to long-time coherent oscillations; in this case, we do not find the rapid thermalization expected by ETH.

The coherent oscillations discussed above are expected to have larger amplitude provided we start from the state  $|\mathbb{Z}_2\rangle$ . To see this, we note that in this case, the wavefunction after  $n$  drive cycles is given by

$$|\psi'(nT)\rangle = \sum_{\alpha} \sum_{p,q} c_{L/2;0}^{\alpha*} c_{p,q}^{\alpha} e^{-i\epsilon_{\alpha} nT/\hbar} |p; q\rangle \quad (32)$$

where  $c_{L/2;0}^{\alpha} = \langle \mathbb{Z}_2 | \alpha \rangle$ . In this case, the leading order contribution to  $O_{22}$  reads

$$O_{22}^{(\mathbb{Z}_2)}(nT) \simeq |c_{L/2;0}^{L/2*}|^2 + c_{L/2;0}^{L/2-1*} c_{L/2-1;1}^{L/2-1} e^{i\Delta nT/\hbar}|^2 \quad (33)$$

which leads to  $O(w_r^2/\Delta^2)$  oscillation amplitude.

In contrast, if one starts from the  $|\mathbb{Z}_2\rangle$  states, the oscillation amplitude is expected to be vanishingly small. This is due to the fact that  $|\mathbb{Z}_2\rangle$  has insignificant overlap with any  $|p_0; q_0\rangle$  state which contributes to  $\langle \hat{n}_2 \hat{n}_4 \rangle$ . We also note that density-density correlation between odd sites (such as  $O_{12}$ ) would show similar behavior for the initial state  $|0\rangle$ ; however, it would have vanishing oscillation amplitude for the  $|\mathbb{Z}_2\rangle$  initial state instead of  $|\mathbb{Z}_2\rangle$ .

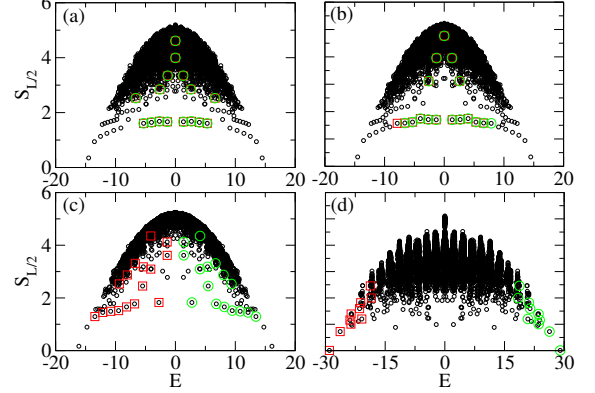


FIG. 13: Plot of the half chain entanglement  $S_{L/2}$  of the eigenstates of  $H_m$  as a function of energy  $E$  for (a)  $\Delta' = 0.005$ , (b) 0.05, (c) 0.5, and (d) 2. The green and red circles indicate states with high overlap with  $|\mathbb{Z}_2\rangle$  and  $|\mathbb{Z}_2\rangle$  respectively. All plots have same Y axes range and correspond to  $L = 24$ . See text for details.

## V. CROSSOVER FROM WEAK TO STRONG STAGGERED DETUNING

In this section, we shall study the behavior of the quasienergy eigenstates as  $\delta E_2/w_r$  is gradually increased. We note at the outset that this behavior can be reproduced by studying the properties of eigenstates of

$$H_m = -(\Delta'/2) \sum_j (-1)^j \sigma_j^z - \sum_j \tilde{\sigma}_j^x \quad (34)$$

such that  $\Delta' \equiv 2\delta E_2/w_r$ . This is due to the fact that a variation of  $\omega_D$  in  $H_F^{(1)}$  can take us close to both the commensuration point where  $\delta E_2 \simeq 0$  (for example, for  $\Delta \simeq 1.2$  and  $\hbar\omega_d \simeq 3.6$ ) and the dynamical freezing point where  $w_r \simeq 0$  (for example, around  $\lambda T/\hbar = 4\pi$ ). We therefore expect this analysis to reveal the nature of the crossover between Hilbert space structure having quantum scars ( $\Delta' = 0$ ) to that having clustering ( $\Delta' \gg 1$ ). Our numerical results are discussed in Sec. V A while a FSA based calculation for scars at small and intermediate value of  $\Delta$  is presented in Sec. V B.

### A. Numerical results for scars

In this section, we first show the entanglement entropy of the eigenstates of  $H_m$  as a function of dimensionless energy  $E$  for four representative values of  $\Delta'$  in Fig. 13. The top left panel of Fig. 13 shows the existence of quantum scars for small  $\Delta' \ll 1$ . These scars which occurs close to the commensuration point where  $x \ll 1$ , have, in accordance with standard expectation, almost equal overlap with  $|\mathbb{Z}_2\rangle$  (red circles) and  $|\mathbb{Z}_2\rangle$  (green circles) states. We find as we increases  $\Delta'$ , the scars with  $E_F < 0$  develops

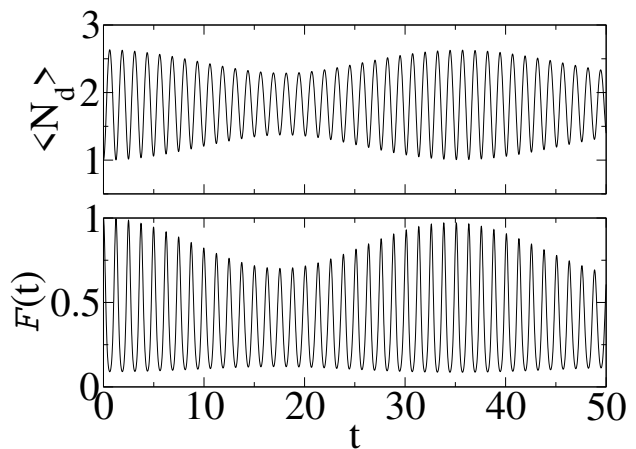
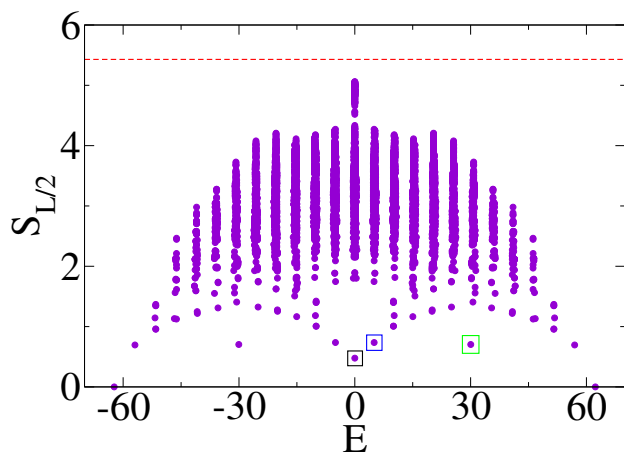


FIG. 15: Left: Plot of  $S_{L/2}$  for eigenstates of  $H_m$  showing the scar states having large overlap with  $|0\rangle$  (black square),  $|1\rangle$  (blue square), and  $|Z_4\rangle$  (green square). The red dashed line indicates the ETH predicted Page value of  $S_{L/2}$ . Right Panel: The dynamics of  $\langle N_d \rangle$  starting from state  $|1\rangle$  (top) and the fidelity  $F(t) = |\langle \psi(t) | 1 \rangle|^2$  (bottom) as a function of time showing scar induced long-time coherent oscillations. For all plots  $L = 24$  and  $\Delta' = 5$ . See text for details.

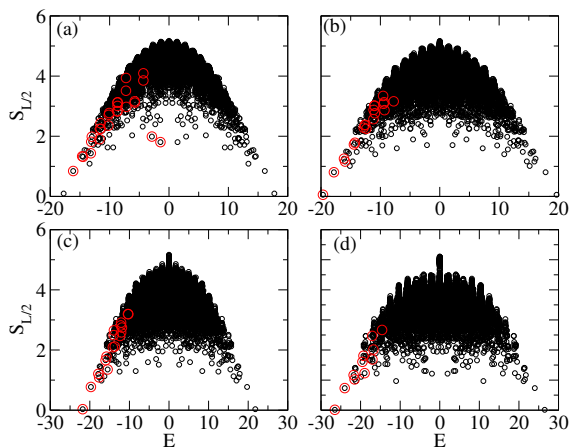


FIG. 14: Plot of the half chain entanglement  $S_{L/2}$  of the eigenstates of  $H_m$  as a function energy  $E$  for (a)  $\Delta' = 0.75$ , (b) 1, (c) 1.25, and (d) 1.75. The red circles indicate states with high overlap with  $|Z_2\rangle$ . All plots have same Y axes range and correspond to  $L = 24$ . See text for details.

higher overlap with  $|Z_2\rangle$  while those with  $E_F > 0$  ex-

These mid-spectrum scar states have no analogue in their counterparts for small  $\Delta'$ . Indeed this can be seen by studying the dynamics of  $\langle N_d \rangle = \langle \sum_j (\sigma_j^z + 1)/2 \rangle$  as a function of time. The fidelity  $F_1 = |\langle 1 | \psi(t) \rangle|^2$  of these oscillations indicate perfect revivals as can be seen from the bottom right panel of Fig. 15. The presence of such oscillations starting from single spin-up state could not have been due to the  $|Z_2\rangle$  scars. Similar oscillatory co-

hibits higher overlap with  $|\bar{Z}_2\rangle$ . This asymmetry can be understood from the fact that the presence of a large  $\Delta'$  pushes the states with high  $|Z_2\rangle$  ( $|\bar{Z}_2\rangle$ ) overlap to lower (higher) quasienergy. For  $\Delta' \gg 1$ , there are almost no mid-spectrum states which has high overlap with either  $|Z_2\rangle$  or  $|\bar{Z}_2\rangle$ . Remarkably, even in this regime, we find existence of scar like states as seen from bottom right panel of Fig. 13; these do not show high overlap with either  $|Z_2\rangle$  or  $|\bar{Z}_2\rangle$ . The crossover between these two situation happens between  $0.75 \leq \Delta' \leq 1$  as can be seen from Fig. 14. Thus at these values of  $\Delta'$ , an almost continuous band of scar states remain although their nature evolves with increasing  $\Delta'$ .

This structure of scars is preserved at higher values of  $\Delta'$  where the Hilbert space is strongly clustered. The mid-spectrum states here do not have significant overlap with either  $|Z_2\rangle$  and  $|\bar{Z}_2\rangle$ . Instead, as we find numerically and as shown in the left panel of Fig. 15, two of these states have high overlap with  $|Z_4\rangle = |\uparrow, \downarrow, \downarrow, \downarrow, \uparrow, \downarrow, \downarrow, \downarrow, \dots\rangle$  states. Other mid spectrum scar states have strong overlap either with the single Rydberg excited state  $|1\rangle = |\uparrow, \downarrow, \downarrow, \dots\rangle$  or the vacuum state  $|0\rangle$  as shown in the left panel of Fig. 15.

herent dynamics with near perfect fidelity revivals is also seen in this regime for initial states  $|0\rangle$  and  $|Z_4\rangle$  as shown in Fig. 16.

The frequencies of these oscillations and the nature of the dynamics starting from the  $|Z_4\rangle$  state can be understood as follows. From the plot of the overlap of the initial state with the Floquet eigenstates, shown in Fig. 17, we find that the overlap of  $|Z_4\rangle$  is maximal with



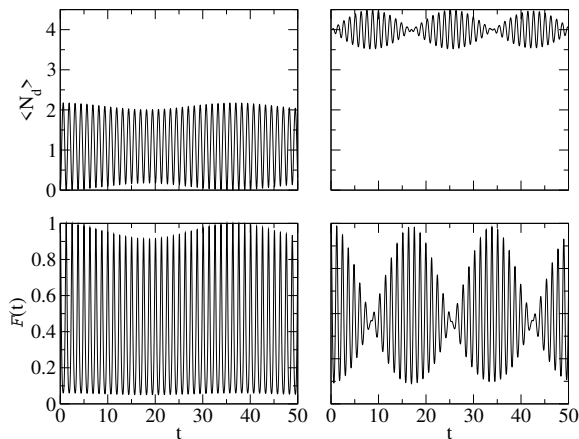


FIG. 16: Left: The dynamics of  $\langle N_d \rangle$  (top) starting from the initial state  $|0\rangle$  and the fidelity  $F(t) = |\langle \psi(t) | 0 \rangle|^2$  (bottom) as a function of time. Right: Similar plots for the initial  $|1\rangle$  state. All left panel plots have same Y axes range as their right panel counterparts. All plots correspond to  $L = 16$  and  $\Delta' = 5$ . See text for details.

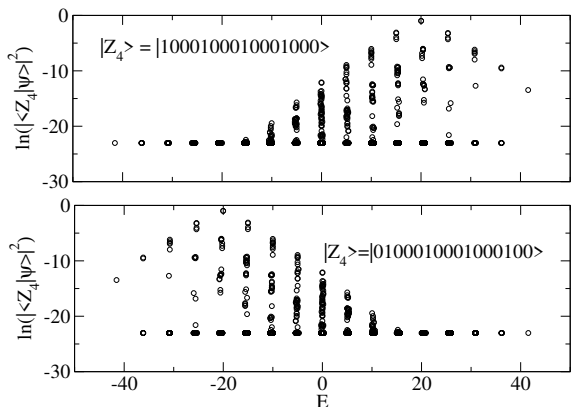


FIG. 17: Plot of  $\ln|\langle Z_4 | n \rangle|^2$  as a function of  $E_F$  for  $|Z_4\rangle$  states which hosts Rydberg excitations on even (top panel) and odd (bottom panel) sites. For all plots  $\Delta' = 5$  and  $L = 16$ . See text for details.

the one of the mid-spectrum scar states. This state has  $E_F > 0$  ( $E_F < 0$ ) if the  $|Z_4\rangle$  hosts Rydberg excitations on odd(even) sites; this is due to the presence of a large  $\Delta'$  in the Hamiltonian which breaks the particle-hole symmetry. The next largest overlap corresponds to two states on both sides of the  $|Z_4\rangle$  states; these have slightly different energies and belong to primary clusters characterized by  $Z_\pi = 5$  and 7 respectively. The difference in energy between the  $Z_4$  scar and these two states leads to the main oscillation frequency  $\omega \simeq \Delta'/(2\hbar)$ ; in addition, the small difference in frequencies of these two states lead to a long-time beating phenomenon as can be seen from the right panel Fig. 16. The analysis of the dynamics starting from  $|1\rangle$  or  $|0\rangle$  reveals a qualitatively similar picture

and we do not discuss them in details here.

The nature of the scar states with large overlap with  $|1\rangle$  states may be qualitatively understood by noting the form of  $H_4^{(1)}$  given in Eq. A.5. For strong  $\Delta'$ , where the analysis of Ref. 52 holds,  $H_4^{(1)}$  is the leading term in  $1/\Delta'$  which induces spin dynamics. Here we note that such a term acting on a state  $|1_j\rangle$  (which represents a single Rydberg excitation on the  $j^{\text{th}}$  site) connects it to  $|1_{j+2}\rangle$ . Thus it creates an almost closed subspace of  $L/2$  such states; the corresponding Floquet eigenstates is therefore expected to have low entanglement and could be a candidate for the scar state having large overlap with  $|1\rangle$ .

A similar, but more complicated holds for scars having large overlap with  $|Z_4\rangle$ . We note that  $H_4^{(1)}$  acting on  $|Z_4\rangle$  connects it to a series of  $L/4$  states where any up-spin state is shifted by two sites. These states are denoted by  $|Z_{4j}\rangle$  and has repeated block of one up-spin on site  $4\ell$  for integer  $\ell$  and three subsequent down-spins. Now let us consider the subsequent action of  $H_4^{(1)}$  on this state; it is easy to see that a further shift of the  $j^{\text{th}}$  up-spin is either forbidden by the constraint or gives back  $|Z_4\rangle$ . This ensures that action of  $H_4^{(1)}$  on  $|Z_{4j}\rangle$  leads to  $L/4 C_2$  new states. Following this argument we find that the dimension of the almost closed subspace formed by the action of  $H_4^{(1)}$  on  $|Z_4\rangle$  is  $\sim \sum_{n=1..L/4} L/4 C_n$ . For finite  $L \leq 24$  studied in our numerics, this leads to a small, almost closed, subspace of states. Thus qualitatively one may expect to have a low-entangled eigenstate formed out of their superposition which have significant overlap with  $|Z_4\rangle$ . We conjecture that such a state may be the  $Z_4$  scar that we find. We also note that this suggests that scars having large overlap with  $|1\rangle$  (for which the closed subspace always has  $O(L)$  states) would be more stable for large  $L$  than their counterparts having large overlap with  $|Z_4\rangle$ .

## B. FSA calculations

To understand the nature of these scars at low and intermediate  $\Delta'$  and the change in their properties as  $\Delta'$  is increased, we use a semi-analytic FSA treatment. To this end, we first note that the presence of the staggered detuning term suggests that such a construction should distinguish between odd and even sites in the lattice. Therefore we adapt the formalism of Ref. 74 which allows for such a sublattice resolved formulation. In this method, the states are labeled by a set of two integers  $n_1$  and  $n_2$  which denotes number of Rydberg excitations (up-spins) on even and odd sites respectively. In what follows we shall construct the matrix elements of  $H_m$  between two such states and then diagonalize this matrix numerically. Such a class of states constitutes a symmetric subspace defined from a set of equivalence classes  $(n_1, n_2)$ ; all elements of these classes are invariant under shuffling of excitations in each sublattice<sup>74</sup>. Thus in this scheme, the action of translation by an even number of

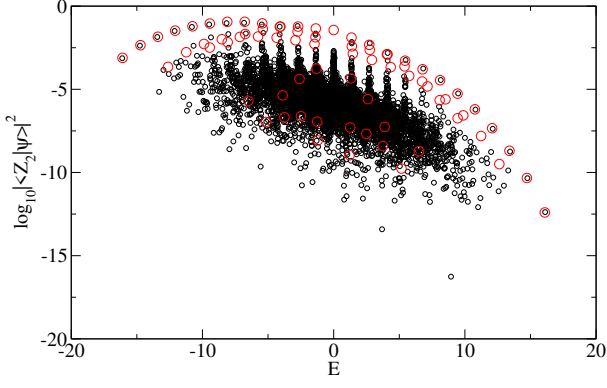


FIG. 18: A plot of  $\log_{10} |\langle \mathbb{Z}_2 | \psi \rangle|^2$  for states obtained via FSA (large red circles) and those obtained from exact numerics (small black circle) for  $\Delta' = 0.5$  and  $L = 24$ . See text for details.

lattice states leads to an equivalent state. The assumption here is that the key information about properties of the states reside in the number of excitation in each sublattice. We note that this procedure naturally yield states which have significant overlap with  $|\mathbb{Z}_2\rangle$  and  $|\bar{\mathbb{Z}}_2\rangle$  since these Neel states are included as elements in the subspace<sup>74</sup>.

The first step towards construction of the matrix elements of  $H_m$  is to construct an orthonormal basis for the symmetric subspace. To this end, we use the prescription of Ref. 74 and write, for a chain with  $2L$  sites

$$|n_1, n_2\rangle = \frac{1}{\mathcal{N}} \sum_a |\alpha_a\rangle \quad (35)$$

$$\mathcal{N} = \frac{(L - n_1 - n_2)L}{(L - n_1)(L - n_2)} \binom{L - n_1}{n_2} \binom{L - n_2}{n_1}$$

where any state  $|\alpha_a\rangle$  contain  $n_1$  and  $n_2$  total Rydberg excitations on even and odd sites respectively. The number of such states,  $\mathcal{N}$ , depends on specific values of  $n_1$  and  $n_2$  and also the Hilbert space constraint of having no two Rydberg excitation on neighboring sites.

The matrix element of  $H_m$  between these states can be easily obtained following the prescription of Ref. 74. To this end, we write, using  $|0\rangle$  as the reference state,

$$\begin{aligned} \langle n_1, n_2 | H_m | m_1, m_2 \rangle &= F_1 + F_2 \\ F_1 &= \Delta' (n_2 - n_1) \delta_{n_1, m_1} \delta_{n_2, m_2} \\ F_2 &= - \left[ M(n_1, n_2) \delta_{m_1, n_1+1} \delta_{m_2, n_2} \right. \\ &\quad \left. + M(n_2, n_1) \delta_{m_1, n_1} \delta_{m_2, n_2+1} \right] + \text{h.c.} \\ M(n_1, n_2) &= \sqrt{\frac{(L - n_1 - n_2)(L - n_1 - n_2 + 1)n_1}{L - n_1}} \end{aligned} \quad (36)$$

We note that the structure of the FSA Hamiltonian suggests that a large  $\Delta'$  essentially separates out states with

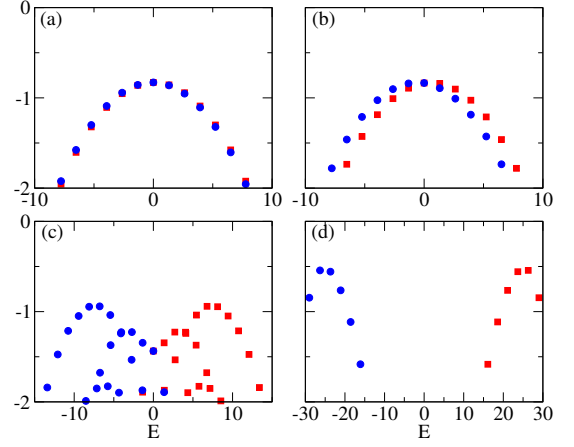


FIG. 19: A plot of  $\log_{10} |\langle \mathbb{Z}_2 | \psi \rangle|^2$  (blue circles) and  $\log_{10} |\langle \bar{\mathbb{Z}}_2 | \psi \rangle|^2$  (red circles) for states obtained via FSA for (a)  $\Delta' = 0.005$ , (b) 0.05, (c) 0.5, and (d) 2. All plots have same Y axes range and correspond to  $L = 24$ . See text for details.

large  $n_1$  from those with large  $n_2$ . Thus the eigenvalues of these Hamiltonian, for large  $\Delta'$ , is expected to have large overlap with either  $|\mathbb{Z}_2\rangle$  or  $|\bar{\mathbb{Z}}_2\rangle$  but not both.

The diagonalization of the FSA matrix constructed from Eq. 36 leads to the eigenvalues of  $H_m$  for a fixed  $\Delta'$ . A comparison of the  $|\mathbb{Z}_2\rangle$  overlap of these states with those of their counterparts obtained via exact numerics for  $L = 24$  and  $\Delta' = 0.5$ , plotted in Fig. 18, shows a near-exact match between the scar eigenstates obtained by these two methods; the eigenstates with  $E_F < 0$  has a much higher overlap with  $|\mathbb{Z}_2\rangle$  compared to those with  $E_F > 0$  in both cases. This allows us to surmise that the present FSA captures the essence of the scar eigenstates in the presence of finite  $\Delta$ .

The overlap between these eigenstates with  $|\mathbb{Z}_2\rangle$  (red dots) and  $|\bar{\mathbb{Z}}_2\rangle$  (blue dots) is shown in Fig. 19. From these, we find that the FSA eigenstates qualitatively reproduce the characteristics of scars seen in exact numerics. For low  $\Delta'$ , the scar states have near exact overlap with both the Neel states (top left panel of Fig. 19); in contrast, as  $\Delta'$  is increased, states with  $E_F > 0$  develop a large overlap with  $|\bar{\mathbb{Z}}_2\rangle$  while those with  $E_F < 0$  overlaps strongly with  $|\mathbb{Z}_2\rangle$ . Thus the crossover of the nature of the scars as a function of  $\Delta'$  is well captured by the FSA. This behavior can be understood to be a consequence of the presence of the diagonal elements of the FSA matrix for finite  $\Delta'$  (Eq. 36); their presence pushes states having large overlap with  $|\mathbb{Z}_2\rangle$  ( $|\bar{\mathbb{Z}}_2\rangle$ ) to opposite ends of the Floquet spectrum. The mid-spectrum scar states at large  $\Delta'$ , however, can not be captured by the present FSA formalism. A more detailed quantitative understanding of such states and their description in terms of a modified FSA approach is left for future studies.

## VI. DISCUSSION

In this work, we have studied a periodically driven Rydberg chain with both uniform and staggered detuning. We have primarily focussed on the limit of large drive amplitude and a square pulse protocol; the uniform detuning term has been made time dependent. We find that the presence of a staggered detuning term leads to several features of the driven system that have no analogue in Floquet dynamics of Rydberg atoms without such a term.

The first of such features involves ergodicity violation of such system via clustering of Floquet eigenstates. We find that when  $\Delta \gg w_r$ , the eigenstates of the Floquet Hamiltonian arrange themselves into several discrete well-separated clusters in the Hilbert space. Each of these clusters belong to definite values of  $Z_\pi$  and the number of such clusters depend on the ratio of  $\hbar\omega_D/\Delta$ . We dub this phenomenon as primary clustering and recognize this to be consequence of near-integrability of  $H_F$  for large  $\Delta/w_r$ . In addition, we also find a secondary clustering which leads to discrete set of states within each of these primary clusters. We tie the presence of such secondary clustering to the existence of emergent conserved quantity,  $Y$ , which was noted earlier in the context of non-driven Rydberg chains with such staggered detuning in Refs. 51,52. We note that these clusterings leading to violation of ETH do not stem from standard Hilbert space fragmentation<sup>57-60</sup> since the Floquet Hamiltonian of the staggered Rydberg chain do not have dynamically disconnected sector at any finite  $w_r$ . Furthermore such clustering is not expected to survive in the thermodynamic limit; however, they will be a feature of finite-sized chains which are typically realized in standard experiments<sup>12,13</sup>.

We also show that the existence of  $Y$  and hence secondary clustering is contingent on incommensuration of the drive frequency and  $\Delta$  which leads to a non-zero  $\delta E_2$ . Thus at commensurate drive frequencies where  $\delta E_2 = 0$ , the secondary clustering is destroyed and states within each primary cluster become ergodic. This is reflected in the values of local observables such as  $O_{22}$  near these commensurate drive frequencies which reach very close to their ETH predicted values. This leads to a possibility of tuning ergodicity properties of the driven system using the drive frequency.

We also study the behavior of the correlation function  $O_{22}$  for the driven chain starting from the vacuum and the Neel states. We find, for initial  $|0\rangle$  and  $|\mathbb{Z}_2\rangle$  dynamical freezing of  $O_{22}$  at specific drive frequencies whose values are well approximated by the analytic Floquet Hamiltonian obtained using FPT. When driven close to these freezing frequencies,  $O_{22}$  starting from  $|0\rangle$  or  $|\mathbb{Z}_2\rangle$  displays oscillations with perfect revivals. The amplitude of these oscillations decreases with increasing  $\Delta$  in the large or intermediate  $\Delta/w_r$  regime; in contrast, their frequencies are pinned to  $\Delta/\hbar$  for both the initial states. We provide a simple qualitative explanation of these features using

the structure of the Floquet eigenstates in this regime. In contrast such oscillations are completely suppressed when the dynamics starts from  $|\bar{\mathbb{Z}}_2\rangle$ ; this leads to a range of drive frequencies where one encounters dynamic freezing. This range increases with  $\Delta$ . We explain this phenomenon qualitatively and point out that the dynamics of  $O_{j2}$ , where  $j$  is odd, would show exactly opposite behavior; it would show range of freezing frequencies for dynamics starting from  $|\mathbb{Z}_2\rangle$  state. This dichotomy is a direct consequence of breaking of the sublattice symmetry by the staggered detuning term.

We have also studied the quantum scars in the Floquet eigenspectrum of such a driven Rydberg chain. Such scars are known to exist for  $\Delta' = 0$ <sup>33</sup> and are dubbed as PXP scars<sup>47</sup>; they have identical overlap with both the Neel states in this limit. We find that with increasing  $\Delta'$ , the scars with energy  $E_F < 0$  develop a stronger overlap with  $|\mathbb{Z}_2\rangle$  while those with  $E_F > 0$  overlap more with  $|\bar{\mathbb{Z}}_2\rangle$ . This phenomenon clearly originates from the breaking of the  $Z_2$  sublattice symmetry due to presence of  $\Delta$ . In fact, at large  $\Delta'$ , we find that no near mid-spectrum scar states have significant overlap with either of the Neel states. Instead, as confirmed from quench dynamics studies in Sec. V, they have a high overlap with either  $|\mathbb{Z}_4\rangle$ , vacuum ( $|0\rangle$ ) or single dipole ( $|1\rangle$ ) states. This indicates that the presence of large  $\Delta'$  leads to scars which have no analog with the standard PXP scars studied earlier in the literature. Our FSA analysis which explains the property of the scars at weak or intermediate  $\Delta'$  fails to capture these mid-spectrum scars at large  $\Delta'$ .

In conclusion, we have shown that a driven Rydberg chain with staggered detuning term leads to several interesting phenomena. These include ergodicity violation via Floquet eigenstate clustering in the strong staggered detuning limit, dynamical freezing, sustained coherent oscillations with perfect revivals near the freezing frequency, existence of separate class of quantum scars with large overlap with  $|0\rangle$ ,  $|1\rangle$  and  $|\mathbb{Z}_4\rangle$  states, and the possibility of tuning ergodicity property of these chains with the drive frequency. The experimental implementation of a Rydberg chain has already been achieved<sup>12,13</sup>; a possible extension of some of these experiments with implementation of staggered detuning may provide a suitable experimental platform testing our theoretical predictions.

### Appendix: Projection operator formalism

In this appendix, we detail the computation of  $Y$  and  $H_2$  using a perturbative formalism developed in Ref. 52. To this end we shall start from a Hamiltonian  $H_m$  (Eq. 34) in the main text and treat  $1/\Delta'$  as the perturbative parameter. In what follows, we write  $H_m = H_0 + H_1$  in terms of  $Z_\pi$  (Eq. 20). This yields

$$H_0 = -\Delta' Z_\pi, \quad H_1 = -\sum_j \tilde{\sigma}_j^x. \quad (\text{A.1})$$

In the rest of this appendix, we shall treat  $H_1$  perturbatively in the regime where  $\Delta' > 1$ .

The formalism used in Ref. 52 constitutes construction of a perturbative effective Hamiltonian for such a system. The method relies on the presence of a canonical transformation, implemented through an operator  $S$ , which yields

$$\begin{aligned} H_{\text{eff}} &= e^{iS} H_m e^{-iS} = H_0 + H^{(1)} + H^{(2)} + \dots \quad (\text{A.2}) \\ H^{(1)} &= [iS, H_0] + H_1 \\ H^{(2)} &= P'[iS, H_1] + \frac{1}{2}[iS, [iS, H_0]]P' \end{aligned}$$

where the ellipsis represents higher order terms and  $P'$  is a projection operator which projects the Hamiltonian to the low-energy manifold of  $H_0$ <sup>52</sup>. The next step is to determine  $S$  to first order in perturbation theory by setting  $H^{(1)} = 0$ . A straightforward calculation using this condition yields

$$iS = \frac{1}{2i\Delta'} \sum_j \tilde{\sigma}_j^y (-1)^j \quad (\text{A.3})$$

Using Eq. A.3, one can now compute  $H^{(2)}$ . While doing this, it is important to remember that the final results needs to be projected in the low-energy manifold of  $H_0$ . This consideration leads to a single term in the second order which can be easily computed by substituting Eq. A.3 in Eq. A.2 given by

$$H^{(2)} = \frac{-1}{\Delta'} Y \quad (\text{A.4})$$

where the expression of  $Y$  is given in Eq. 24 of the main text. We note that as long as the perturbation theory is valid  $Y$  emerges as a constant of motion; however, this breaks down, along with the perturbative approach, when  $\Delta' \rightarrow 0$ .

The higher order terms in the perturbation theory can be computed systematically using this approach and is detailed out in Ref. 52. This yields  $H^{(3)} = 0$ ; the leading order non-zero term is given by  $H^{(4)}$ . As shown in Ref. 52, this can be written as

$$\begin{aligned} H^{(4)} &= H_1^{(4)} + H_2^{(4)} \\ H_1^{(4)} &= \frac{-1}{2\Delta'^3} \sum_j (-1)^j (\tilde{\sigma}_j^+ \tilde{\sigma}_{j+2}^- + \text{h.c.}) \quad (\text{A.5}) \\ H_2^{(4)} &= \frac{-1}{2\Delta'^3} \sum_j P_{j-1} \sigma_j^z P_{j+1} P_{j+2} + P_{j-2} P_j - \sigma_j^z P_{j+1} \\ &\quad - 2P_{j-1} \sigma_j^z P_{j+1} \end{aligned}$$

We note that  $H_1^{(4)}$  is the leading order term introducing non-trivial spin dynamics. The expression of  $H_1^{(4)}$  has been used in Sec. V of the main text for developing a qualitative understanding of the  $|\mathbb{Z}_4\rangle$  and single-dipole scar states.

- 
- <sup>1</sup> A. Polkovnikov, K. Sengupta, A. Silva, and M. Vengalattore, *Rev. Mod. Phys.* **83**, 863 (2011).  
<sup>2</sup> D. Ziarnaga, *Adv. Phys.* **59**, 1063 (2010).  
<sup>3</sup> A. Dutta, G. Aeppli, B. K. Chakrabarti, U. Divakaran, T. F. Rosenbaum, and D. Sen, *Quantum phase transitions in transverse field spin models: from statistical physics to quantum information* (Cambridge University Press, Cambridge, 2015).  
<sup>4</sup> S. Mondal, D. Sen, and K. Sengupta, *Quantum Quenching, Annealing and Computation*, edited by A. Das, A. Chandra, and B. K. Chakrabarti, *Lecture Notes in Physics* **802**, 21 (Springer, Berlin, Heidelberg, 2010); C. De Grandi and A. Polkovnikov, *ibid*, **802**, 75.  
<sup>5</sup> M. Bukov, L. D'Alessio and A. Polkovnikov, *Advances in Physics* **64**, 139 (2015).  
<sup>6</sup> L. D'Alessio and A. Polkovnikov, *Ann. Phys.* **333**, 19 (2013).  
<sup>7</sup> L. D'Alessio, Y. Kafri, A. Polokovnikov, and M. Rigol, *Adv. Phys.* **65**, 239 (2016).  
<sup>8</sup> A. Sen, D. Sen, and K. Sengupta, *J. Phys. Cond. Mat.* **33**, 443003 (2021).  
<sup>9</sup> I. Bloch, J. Dalibard, and W. Zwerger, *Rev. Mod. Phys.* **80**, 885 (2008); L. Taurell and L. Sanchez-Palencia, *C. R. Physique* **19**, 365 (2018).  
<sup>10</sup> M. Greiner, O. Mandel, T. Esslinger, T. W. Hansch, and I. Bloch, *Nature (London)* **415**, 39 (2002); C. Orzel, A. K. Tuchman, M. L. Fenselau, M. Yasuda, and M. A. Kasevich, *Science* **291**, 2386 (2001).  
<sup>11</sup> T. Kinoshita, T. Wenger, and D. S. Weiss, *Nature (London)* **440**, 900 (2006); L. E. Sadler, J. M. Higbie, S. R. Leslie, M. Vengalattore, and D. M. Stamper-Kurn, *Nature (London)* **443**, 312 (2006).  
<sup>12</sup> W. Bakr, J. Gillen, A. Peng, S. Foelling and M. Greiner, *Nature* **462**, 74 (2009); W. S. Bakr, A. Peng, M. E. Tai, R. Ma, J. Simon, J. I. Gillen, S. Folling, L. Pollet, and M. Greiner, *Science* **329**, 547 (2010).  
<sup>13</sup> H. Bernien, S. Schwartz, A. Keesling, H. Levine, A. Omran, H. Pichler, S. Choi, A. S. Zibrov, M. Endres, M. Greiner, V. Vuletic, and M. D. Lukin, *Nature (London)* **551**, 579 (2017); H. Levine, A. Keesling, A. Omran, H. Bernien, S. Schwartz, A. S. Zibrov, M. Endres, M. Greiner, V. Vuletic, and M. D. Lukin, *Phys. Rev. Lett.* **121**, 123603 (2018).  
<sup>14</sup> T. Kitagawa, E. Berg, M. Rudner, and E. Demler, *Phys. Rev. B* **82**, 235114 (2010); N. H. Lindner, G. Refael, and V. Galitski, *Nat. Phys.* **7**, 490 (2011); T. Kitagawa, T. Oka, A. Brataas, L. Fu, and E. Demler, *Phys. Rev. B* **84**, 235108 (2011).  
<sup>15</sup> M. Thakurathi, A. A. Patel, D. Sen, and A. Dutta, *Phys. Rev. B* **88**, 155133 (2013); A. Kundu, H. A. Fertig, and B.

- Seradjeh, Phys. Rev. Lett. **113**, 236803 (2014).
- <sup>16</sup> F. Nathan and M. S. Rudner, New J. Phys. **17**, 125014 (2015); B. Mukherjee, A. Sen, D. Sen, and K. Sengupta, Phys. Rev. B **94**, 155122 (2016); B. Mukherjee, P. Mohan, D. Sen, and K. Sengupta, Phys. Rev. B **97**, 205415 (2018).
- <sup>17</sup> T. Nag, S. Roy, A. Dutta, and D. Sen, Phys. Rev. B **89**, 165425 (2014); T. Nag, D. Sen, and A. Dutta, Phys. Rev. A **91**, 063607 (2015).
- <sup>18</sup> A. Agarwala, U. Bhattacharya, A. Dutta, and D. Sen, Phys. Rev. B **93**, 174301 (2016); A. Agarwala and D. Sen, Phys. Rev. B **95**, 014305 (2017).
- <sup>19</sup> D. J. Luitz, Y. Bar Lev, and A. Lazarides, SciPost Phys. **3**, 029 (2017); D. J. Luitz, A. Lazarides, and Y. Bar Lev, Phys. Rev. B **97**, 020303 (2018).
- <sup>20</sup> R. Ghosh, B. Mukherjee, and K. Sengupta Phys. Rev. B **102**, 235114(2020).
- <sup>21</sup> M. Heyl, A. Polkovnikov, and S. Kehrein, Phys. Rev. Lett. **110**, 135704 (2013); For a review, see M. Heyl, Rep. Prog. Phys **81**, 054001 (2018).
- <sup>22</sup> A. Sen, S. Nandy, and K. Sengupta, Phys. Rev. B **94**, 214301 (2016); S. Nandy, K. Sengupta, and A. Sen, J. Phys. A: Math. Theor. **51**, 334002 (2018); M. Sarkar and K. Sengupta, Phys. Rev. B **102**, 235154 (2020).
- <sup>23</sup> S. Aditya, S. Samanta, A. Sen, K. Sengupta, and D. Sen, arXiv:2112.02915 (unpublished); A. A. Makki, S. Bandyopadhyay, S. Maity, and A. Dutta, arXiv:2112.02930 (unpublished).
- <sup>24</sup> V. Khemani, A. Lazarides, R. Moessner, and S. L. Sondhi, Phys. Rev. Lett. **116**, 250401 (2016).
- <sup>25</sup> D. V. Else, B. Bauer, and C. Nayak, Phys. Rev. Lett. **117**, 090402 (2016).
- <sup>26</sup> J. Zhang, P. W. Hess, A. Kyprianidis, P. Becker, A. Lee, J. Smith, G. Pagano, I-D. Potirniche, A. C. Potter, A. Vishwanath, N. Y. Yao, and C. Monroe, Nature (London) **543**, 217 (2017).
- <sup>27</sup> A. Das, Phys. Rev. B **82**, 172402 (2010).
- <sup>28</sup> S. Bhattacharyya, A. Das, and S. Dasgupta, Phys. Rev. B **86**, 054410 (2010).
- <sup>29</sup> S. Hegde, H. Katiyar, T. S. Mahesh, and A. Das, Phys. Rev. B **90**, 174407 (2014).
- <sup>30</sup> S. Mondal, D. Pekker, and K. Sengupta, Europhys. Lett. **100**, 60007 (2012).
- <sup>31</sup> U. Divakaran and K. Sengupta, Phys. Rev. B **90**, 184303 (2014); B. Mukherjee.
- <sup>32</sup> B. Mukherjee, A. Sen, D. Sen and K. Sengupta, Phys. Rev. B **102**, 075123 (2020).
- <sup>33</sup> B. Mukherjee, S. Nandy, A. Sen, D. Sen and K. Sengupta, Phys. Rev. B **101**, 245107 (2020).
- <sup>34</sup> S. Nandy, A. Sen, and D. Sen, Phys. Rev. X **7**, 031034 (2017).
- <sup>35</sup> S. Nandy, A. Sen, and D. Sen, Phys. Rev. B **98**, 245144 (2018).
- <sup>36</sup> B. Mukherjee, A. Sen, D. Sen, and K. Sengupta, Phys. Rev. B **102**, 014301 (2020).
- <sup>37</sup> J. M. Deutsch, Phys. Rev. A **43**, 2046 (1991).
- <sup>38</sup> M. Srednicki, Phys. Rev. E **50**, 888 (1994); *ibid.*, J. Phys. A **32**, 1163 (1999).
- <sup>39</sup> M. Rigol, V. Dunjko, and M. Olshanii, Nature (London) **452**, 854 (2008).
- <sup>40</sup> L. D'Alessio and M. Rigol, M. Phys. Rev. X **4**, 041048 (2014).
- <sup>41</sup> D. M. Basko, I. L. Aleiner, B. L. Altshuler, Ann. Phys. **321**, 1126-1205 (2006).
- <sup>42</sup> R. Nandkishore and D. A. Huse Ann. Rev. Cond. Mat. **6**, 15 (2015).
- <sup>43</sup> F. Alet and N. Laflorencie, Comptes Rendus Physique **19**, 498 (2018).
- <sup>44</sup> D. A. Abanin, E. Altman, I. Bloch, and M. Serbyn, Rev. Mod. Phys. **91**, 021001 (2019).
- <sup>45</sup> D-L Deng, S. Ganesan, X. Li, R. Modak, S. Mukerjee, and J. H. Pixley, Ann. Phys. (Berlin) **529**, 1600399 (2017).
- <sup>46</sup> C. J. Turner, A. A. Michailidis, D. A. Abanin, M. Serbyn, and Z. Papic, Z. Nat. Phys. **14**, 745 (2018).
- <sup>47</sup> C. J. Turner, A. A. Michailidis, D. A. Abanin, M. Serbyn, and Z. Papic, Phys. Rev. B **98**, 155134 (2018).
- <sup>48</sup> K. Bull, I. Martin, and Z. Papic, Phys. Rev. Lett. **123**, 030601 (2019).
- <sup>49</sup> V. Khemani, C. R. Lauman, and A. Chandran, Phys. Rev. B **99**, 161101 (2019).
- <sup>50</sup> S. Maudgalya, N. Regnault, and B. A. Bernevig, Phys. Rev. B **98**, 235156 (2018).
- <sup>51</sup> T. Iadecola, M. Schecter, and S. Xu, Phys. Rev. B **100**, 184312 (2019).
- <sup>52</sup> I-C Chen and T. Iadecola, Phys. Rev. B **103**, 214304 (2021).
- <sup>53</sup> N. Shiraishi, arXiv:1904.05182
- <sup>54</sup> M. Schecter and T. Iadecola, Phys. Rev. B **98**, 035139 (2018).
- <sup>55</sup> P. A. McClarty, M. Haque, A. Sen, and J. Richter, Phys. Rev. B **102**, 224303 (2020).
- <sup>56</sup> D. Banerjee and A. Sen, Phys. Rev. Lett. **126**, 220601 (2021).
- <sup>57</sup> S. Pai, M. Pretko, and R. M. Nandkishore, Phys. Rev. X **9**, 021003 (2019); V. Khemani, M. Hermele, and R. Nandkishore, Phys. Rev. B **101**, 174204 (2020).
- <sup>58</sup> P. Sala, T. Rakovszky, R. Verresen, M. Knap, and F. Pollmann, Phys. Rev. X **10**, 011047 (2020); S. Moudgalya, A. Prem, R. Nandkishore, N. Regnault, and B. A. Bernevig, arXiv:1910.14048.
- <sup>59</sup> Z.-C. Yang, F. Liu, A. V. Gorshkov, and T. Iadecola, Phys. Rev. Lett. **124**, 207602 (2020); G. De Tomasi, D. Hetterich, P. Sala, and F. Pollmann, Phys. Rev. B **100**, 214313 (2019).
- <sup>60</sup> B. Mukherjee, D. Banerjee, K. Sengupta and A. Sen, Phys. Rev. B **104**, 155117 (2021).
- <sup>61</sup> S. Coleman, R. Jackiw, and L. Susskind, Ann. Phys. **93**, 267 (1975)
- <sup>62</sup> S. Coleman, Ann. Phys. (N.Y.) **101**, 239 (1976).
- <sup>63</sup> S. Chandrasekharan and U. J. Wiese, Nucl. Phys. B **492**, 455 (1997); U. J. Wiese, Ann. Phys. (Amsterdam) **525**, 777 (2013).
- <sup>64</sup> E. Zohar, I. I. Cirac, and B. Reznik, Rep. Prog. Phys. **79**, 014401 (2016)
- <sup>65</sup> R. Brower, S. Chandrasekharan, and U. Wiese, Phys. Rev. D **60**, 094502 (1999); R. Brower, S. Chandrasekharan, S. Riederer, and U. Wiese, Nucl. Phys. B **693**, 149 (2004).
- <sup>66</sup> M. Dalmonte and S. Montangero, Contemp. Phys. **57**, 388 (2016).
- <sup>67</sup> D. Banerjee, M. Dalmonte, M. Müller, E. Rico, P. Stebler, U.-J. Wiese, and P. Zoller, Phys. Rev. Lett. **109**, 175302 (2012); D. Banerjee, M. Bogli, M. Dalmonte, E. Rico, P. Stebler, U. J. Wiese, and P. Zoller Phys. Rev. Lett. **110**, 125303 (2013).
- <sup>68</sup> A. Celi, B. Vermersch, O. Viyuela, H. Pichler, M. D. Lukin, and P. Zoller, Phys. Rev. X **10**, 021057 (2020).
- <sup>69</sup> A. J. A. James, R. M. Konik, and N. J. Robinson, Phys. Rev. Lett. **122**, 130603 (2019).
- <sup>70</sup> I-C Chen and T. Iadecola, Phys. Rev. B **103**, 214304



- (2021)
- <sup>71</sup> F. M. Surace, P. P. Mazza, G. Giudici, A. Leroise, A. Gambassi, and M. Dalmonte, Phys. Rev. X **10**, 021041 (2020).
- <sup>72</sup> S. Sachdev, K. Sengupta, and S. M. Girvin, Phys. Rev. B **66**, 075128 (2002).
- <sup>73</sup> P. Fendley, K. Sengupta, and S. Sachdev, Phys. Rev. B **69**, 075106 (2004).
- <sup>74</sup> C. J. Turner, J.-Y. Desaulles, K. Bull, and Z. Papic, Phys. Rev X **11**, 021021 (2021).